ASSEMBLY OF NANOSTRUCTURES

IN III-V SEMICONDUCTOR FILMS

by

Jennifer Y. Lee-Feldman

A dissertation submitted in partial fulfillment
of the requirements for the degree of
Doctor of Philosophy
(Materials Science and Engineering)
in The University of Michigan
2010

Doctoral Committee:

Associate Professor Joanna Mirecki-Millunchick, Chair
Professor Brian J. Love
Professor Peter S. Smereka
Associate Professor Christopher A. Pearson

© Jennifer Y. Lee-Feldman, 2010

DEDICATION

This dissertation is dedicated to my family

and

my partner, Arthur.

ACKNOWLEDGMENTS

Special thanks to Arvind Baskaran, Emine Cagin, Aaron Dehne, Kevin Grossklaus, Min W. Kim, Pei-Cheng Ku, Divine Kumah, Luke Lee, Hugh McKay, Chipo Mulaisho, Ben Norman, Mark Noordhoek, Chris Pearson, Paul Rudzinski, Tim Saucer, Vanessa Sih, Peter Smereka, and Haiping Sun for all their assistance in making this research possible.

This research was supported by NSF Grant No. DMR 0307938 and Sandia National Labs (763642).

TABLE OF CONTENTS

DEDICATION .... **ii**

ACKNOWLEDGMENTS .... **iii**

LIST OF FIGURES .... **vii**

LIST OF TABLES .... **xi**

CHAPTER 1 – Introduction **1**

Growth Modes *2*

Strain Relaxation *3*

Quantum Dot Growth *4*

Focused Ion Beams *5*

References *7*

CHAPTER 2 – Experimental Procedures **10**

Sample Preparation *10*

FIB Surface Processing *11*

FIB for TEM Lift-Out *13*

Image Analysis *14*

Photoluminescence Measurements *15*

CHAPTER 3 – Very Thin Strained Films **17**

Background 17

Experimental Details..20

Results 21

Effect of Ga Growth Rate..21

Effect of Growth Temperature 22

Intermixing: COBRA Results 27

Mathematical Model..29

Effect of As Overpressure 32

Conclusions 35

References 37

CHAPTER 4 – FIB-Induced InAs Quantum Dots 39

Background 40

Simulations of III-V Growths..40

Substrate Oxide Desorption...41

Formation of Quantum Dots..42

Ex Situ Methods 42

In Situ Methods 44

Kinetic Monte Carlo Simulations 46

Experimental Details..50

Results 51

Ex Situ FIB Processing 51

In Vacuo Quantum Dot Arrays...56

Fidelity 56

Changing Growth Temperature 61

Filling of Holes..62

Hole and Quantum Dot Size 66

Changing Periodicity 67

Conclusions *71*

References *73*

CHAPTER 5 – Optoelectronic Properties of FIB-Induced InAs Quantum Dots......76

Background *77*

PL of Assembled Dots..77

TEM to Investigate Defects..78

Photoluminescence Results *79*

Cross-Sectional TEM *85*

Conclusions *87*

References *89*

CHAPTER 6 – Conclusions 92

Discussion of Work..*92*

Future Experiments...*93*

References *97*

LIST OF FIGURES

Figure 2.1: Schematic of the combined MBE, STM, and FIB systems............................12

Figure 2.2: Shows a typical FIB-milled sample area that is approximately 100 × 100 μm^2. In this image B is a designation physically milled onto the substrate. 13

Figure 2.3: A typical scanning tunneling microscopy image of 2 ML GaAs film on $In_{0.53}Ga_{0.47}As$/InP with the edges selected using the histogram on the right. 15

Figure 3.1: Cross-sectional TEM dark field image of lateral composition modulation of a $GaAs_{2ML}$ / $GaSb_{2ML}$ short period superlattice. 18

Figure 3.2: STM images of the first 5, 10, and 15 periods of a GaAs/InAs short period superlattice. 19

Figure 3.3: STM image of lattice-matched $In_{0.53}Ga_{0.47}As$ buffer layer on InP(001) upon which 2 ML thick GaAs films are grown. 21

Figure 3.4: STM images of various Ga growth rates for 2 ML of GaAs on InGaAs / InP: R_{Ga}= (a) 0.05, (b) 0.10, (c) 0.20, and (d) 0.40 ML/s with a constant F_{As}=1.5 ML/s. 22

Figure 3.5: Series of STM images for 2 ML thick GaAs films on lattice-matched $In_{0.53}Ga_{0.47}As$/InP grown with R_{Ga}=0.05 ML/s and F_{As}=1.5 ML/s at T= (a) 420, (b) 480, and (c) 540 °C. 23

Figure 3.6: Arrhenius plot of the edge densities N as a function of inverse T for 2 ML thick GaAs films on lattice-matched $In_{0.53}Ga_{0.47}As$/InP deposited with F_{As}=1.5 ML/s at R_{Ga}=0.2 ML/s and R_{Ga}=0.05 ML/s. 26

Figure 3.7: STM images of 2 ML GaAs films on lattice-matched $In_{0.53}Ga_{0.47}As$/InP grown at T = (a) 480 °C and (b) 520 °C. 27

Figure 3.8: COBRA occupancy profiles align closely with STM height profiles of samples grown at (a) 480 °C and (b) 520 °C. 28

Figure 3.9: COBRA results of (a) In content and (b) strain as a function of the distance from the top most layers. 29

Figure 3.10: Arrhenius plot of the edge densities *N* as a function of inverse *T* for 2 ML GaAs films on lattice-matched $In_{0.53}Ga_{0.47}As$/InP deposited with F_{As}=1.5 ML/s at R_{Ga}=0.2 ML/s and R_{Ga}=0.05 ML/s. Calculated Ga adatom densities η_{Ga} are shown as lines (dotted for R_{Ga}=0.05 ML/s and dashed for R_{Ga}=0.2 ML/s). 32

Figure 3.11: (a) Plot of the edge densities N as a function of F_{As}:R_{Ga} for 2 ML thick GaAs films on lattice-matched $In_{0.53}Ga_{0.47}As$/InP deposited at *T*=480 °C. Calculated Ga adatom densities η_{Ga} are shown as lines (dotted for R_{Ga}=0.05 ML/s and dashed for F_{As}=1.5 ML/s). Representative STM images are shown for the growth conditions such that the F_{As}:R_{Ga} ratio of 15:1 is the same: (b) was grown with R_{Ga}=0.05 ML/s and F_{As}=0.75 ML/s, and (c) was grown with R_{Ga}=0.1 ML/s and F_{As}=1.5 ML/s. 33

Figure 3.12: STM images for 2 ML thick GaAs films on lattice-matched $In_{0.53}Ga_{0.47}As$/InP grown with R_{Ga} of 0.05 ML/s at *T*= 520 °C and F_{As} of 1.0 ML/s, and with (a) As tetramers, As_4, and (b) As dimers As_2. 35

Figure 4.1: Elastic KMC simulation results as a function of deposition of InAs with the same growth parameters and starting morphology. The width of the computational cell is 128 a.u. 48

Figure 4.2: Elastic KMC simulation results for (a) varying temperature, (b) varying diameter, (c) varying depth, and (d) varying wall slope (gradual = 23°, abrupt = 74° with respect to the surface) of 0.5 ML InAs deposited on GaAs. The number of dots is for an average of at least 4 different randomizations. The width of the computational cell is 128 a.u. 49

Figure 4.3: AFM images of (a) typical thermal desorption at 620 °C with rms roughness of 1.8 nm and (b) a 4 ML Ga-assisted oxide desorption with rms roughness of 0.68 nm. 52

Figure 4.4: AFM images of (a) and (b) 1.8 ML InAs on *ex situ* FIB-treated GaAs that were desorbed in the MBE chamber with As overpressure. The FIB processing of (a) has hole spacings of 30 nm and dwell time of 28 μs and (b) has hole spacings of 280 nm and dwell time of 2270 μs. 53

Figure 4.5: AFM image of 1.8 ML InAs on top of 20 nm GaAs buffer grown on Ga-assisted desorbed GaAs. 55

Figure 4.6: AFM image of a GaAs buffer layer that has been patterned with an array of holes spaced 250 nm apart and dosed with a dwell time of 800 μs per hole, followed by annealing at *T*=530 °C under low As_4 flux. The height scale is 3 nm. 57

Figure 4.7: Probability of finding a hole, single quantum dot, or multiple quantum dots appearing at the intended location for a 2.0 ML-thick InAs film deposited at 530 °C for arrays with periodicity of 140 nm (green triangle), 275 nm (red square), 500 nm (black circle), and 550 nm (blue diamond). 58

Figure 4.8: AFM images of a 2.0 ML InAs film deposited at T=530 °C on GaAs upon hole arrays patterned 250 nm apart and at dwell times of (a) 560 μs and (b) 1500 μs. The height scale is 10 nm. The dotted circle in (b) indicates the presence of a quantum dot next to the irradiated hole it nucleated from. 59

Figure 4.9: Plot of the feature (a) diameter and (b) height as a function of dwell time for holes (open circles) and quantum dots (closed circles) from 2.0 ML InAs deposited at 530 °C. 60

Figure 4.10: AFM image of a 1.8 ML-thick InAs film upon a pattern of holes spaced 140 nm apart and exposed to the beam 1600 μs per spot. The height scale is 15 nm. 61

Figure 4.11: AFM images of FIB-modified arrays of GaAs at different periodicities and varying levels of InAs deposition. 63

Figure 4.12: Average area of holes as a function of dwell time for the spacing of 560 nm. 64

Figure 4.13: Average line profile of a hole filled by 0.9 ML InAs for 1200 μs dwell time and 560 nm spacing. 66

Figure 4.14: Depths and widths for holes, 0.9 ML InAs, and 1.5 ML InAs. Left: dwell time=1200 μs; right: dwell time=2000 μs 69

Figure 4.15: AFM images of 1.5 ML InAs on GaAs with a FIB dwell time of 2000 μs at different hole spacings (a) 100, (b) 140, (c) 280, and (d) 560 nm. 70

Figure 4.16: Average quantum dot height and width varied by periodicity at a constant dwell time of 1200 μs. 71

Figure 5.1: Cross-sectional schematic of PL samples grown with GaAs/AlAs superlattices................................80

Figure 5.2: AFM images of uncapped 1.8 ML InAs on FIB modified surfaces of 30 nm spacing and dwell times of (a) 30, (b) 20, and (c) 15 μs. 81

Figure 5.3: Using the Ku PL setup (532 nm wavelength with 15 mW power at 77 K), (a) an overview of the sample surface where FIB irradiation occurred and (b)

the resulting PL within those areas. C, B, and A in (a) refer to FIB irradiated areas with 30 nm spacing with a 30 kV, 7.5 pA ion beam and dwell times of 10, 20, and 30 μs respectively....82

Figure 5.4: Using the Sih PL setup (730 nm wavelength with 0.4 mW power at 10 K), (a) Overview of the sample surface where FIB irradiation occurred and (b) the resulting PL within those areas. C, B, and A in (a) refer to FIB irradiated areas with 30 nm spacing with a 30 kV, 7.5 pA ion beam and dwell times of 10, 20, and 30 μs respectively....83

Figure 5.5: Two different PL spatial maps of the InAs quantum dot peak taken at various positions across the FIB-irradiated areas using a fast steering mirror. 84

Figure 5.6: Bright field TEM image (2-beam 002 type) of a cross section of the FIB-irradiated PL sample with defects at the interface, a stacking fault, and a dislocation loop marked....86

Figure 5.7: Bright field TEM image (2-beam 220 type) of a cross section of the FIB-irradiated PL sample with dislocation dipoles at the interface and below the interface....86

Figure 5.8: Bright field TEM image (2-beam 002 type) of a cross section of the FIB-irradiated PL sample. The images show (a) triangle-shaped defects at the interface or below it and (b) higher resolution image of the defect below the interface. These are most likely stacking faults....87

Figure 6.1: STM images of 2 ML on $In_{0.53}Ga_{0.47}As$ / InP(001). 94

LIST OF TABLES

Table 1.1: Lattice constants for relevant III-V semiconductors. 4

Table 3.1: Average mesa width determined from STM images for 2 ML thick GaAs films on lattice-matched $In_{0.53}Ga_{0.47}As$/InP grown at various temperatures with R_{Ga}=0.05 ML/s and F_{As}=1.5 ML/s. 24

Table 5.1: Bandgap energies and corresponding PL wavelength emission for relevant III-V semiconductors at 0 K. 76

CHAPTER 1 – Introduction

Heteroepitaxially-grown III-V compound semiconductor films are of great technological importance in a variety of electronic[1] and optoelectronic[2] applications. The major technological challenge in developing these devices is to balance the theoretical efficiency gains of moving towards smaller features sizes against the practical performance attenuation due to device sensitivity to changes in microstructure and morphology at such small scales. During epitaxial film growth, there is a threshold at which planar growth transitions to three-dimensional islanding. Either growth scenario can be useful, as some device structures require smooth films[3], and others utilize self-assembled islands to form quantum dots[4-6]. These structural features can only be effectively exploited if they can be reliably controlled and positioned within a complex device structure. Device structure, and ultimately device performance, depends greatly on the growth conditions of the film—notably the growth temperature and the ratio of the group V flux to the group III flux.[7] It is possible to direct the assembly of nanostructures, leading to precise placement and reliable dimensions of structural growth by using self-ordering mechanisms[8] or to more actively direct growth by patterning the surface[9].

This work investigates the effects of self assembly and directed assembly in III-V semiconductor growth. The goal of this work is to characterize surface features in order

to reproduce them again reliably. Once the growth parameters for features are well defined, then greater care can be taken to reduce the variation in feature geometry and composition. In this way, future growths can be precisely calibrated for integration in devices.

Chapter 1 introduces the interest in the growth of III-V semiconductors and provides additional background information necessary to understand the growth mechanisms involved. Chapter 2 describes the experimental techniques employed throughout the study. In the chapters 3 and 4 we directly assemble features by both changing growth parameters to allow for regular ordering and then by inserting patterned surfaces to control positioning and sizes. We also investigate the growth mechanisms of these orderings to understand the physics behind the assembly. Chapter 3 investigates the changes in ordering of morphologies of very thin strained films for many different growth conditions. Chapter 4 uses focused ion beam (FIB) surface modification techniques to place InAs QDs on GaAs and also discusses the initial nucleation. We also examine the potential for device integration by examining the optoelectronic characteristics of samples in Chapter 5. The last chapter, Chapter 6, provides a review of the findings of the entire work and suggests directions for further studies.

Growth Modes

In order to create assembled features one must understand the growth mechanisms of films. For both homogeneous and heterogeneous epitaxial growth, the resultant thin films depend highly on the interactions between the substrate and adatoms deposited. There are three main growth modes: Frank-van der Merwe (FM), Volmer-Weber (VW),

and Stranski Krastanov (SK).[10] The FM mode is characterized as layer-by-layer growth, where adatoms preferentially bond to the surface and fill in completely before the next layer to create a very smooth surface. FM growth is often associated with homoepitaxial films. In VW growth, islanding occurs as a result of adatom-adatom interactions being more favorable than the adatoms to the surface, usually resulting from strain. The SK growth mode is a combination of FM and VW growth modes: two-dimensional layers and three-dimensional islands. There is a critical thickness where growth transitions from layer-by-layer (FM) to island formation (SK) that depends on the surface energy difference and strain between the film and substrate. The smooth layer formed before the critical thickness is achieved is called the wetting layer.

Strain Relaxation

The SK growth mode is an example of how surface morphologies are altered by elastic strain energy[4, 11-15] arising due to lattice mismatch. The misfit between the film and substrate is so high that islands nucleate to relieve the strain.

Strain relaxation is explained by the Asaro-Tiller-Grinfield (ATG) instability[16-19]. It shows that an undulation forms on the surface in order to elastically relax the film. This reduction in energy is counteracted by the surface energy required to form the undulation. The wavelength of the instability is proportional to γ/ε^2, where γ is the surface energy and ε is the misfit strain. The amplitude of these undulations, however, is dictated by the mass transport, or diffusivity, of atoms on the surface. The ATG instability has been shown in different growth features: islands, trenches[20], surface cusps[21], and cracks[22].

The material systems used in this work have a large amount of strain, which have been tabulated in Table 1.1. Specifically we look at two systems: GaAs on $In_{0.53}Ga_{0.47}As$ that is lattice matched to InP with strain of 3.70%, and InAs on GaAs with strain of 7.16%. The concepts and mechanisms from these materials can also be applied to other similar systems, such as AlAs on InP, or GaSb on GaAs.

Material	Lattice Constant *a* (Å)	Strain ε (%) on InP
GaAs	5.653	3.70
AlAs	5.661	3.56
InP	5.870	n/a
InAs	6.058	3.20
GaSb	6.096	3.85

Table 1.1: Lattice constants for relevant III-V semiconductors.[23]

Quantum Dot Growth

An important feature of quantum dots is their ability to self assemble. Epitaxial stress from lattice mismatch between the film and substrate cause the quantum dots to form. The alignment of InAs quantum dots into regular and dense arrays is vigorously pursued for applications in optoelectronics[24, 25] and cryptography[26, 27]. Extensive studies of the optimization of the growth conditions of quantum dots have been performed.[28-31] Quantum dots have been placed in quantum wells[32, 33], grown on cleaved surfaces[34], and stacked in repeated structures[28, 35].

There are a variety of schemes to actively control the nucleation locations of the dots, ranging from standard lithographic techniques[36-38] to mechanical deformation of

the surface[39]. *In situ* FIB patterning has the capability of creating patterns on the order of a few hundred nanometers or less, without the need for *ex situ* processing.[40-42] As such, FIB patterning has emerged as a viable tool for the fabrication of photonic and optoelectronic devices[43, 44] and as a characterization tool used in conjunction with scanning electron microscopy (SEM) and transmission electron microscopy (TEM)[45]. The FIB is advantageous over other lithographic techniques because of smaller feature resolution, the freedom from masks, and the versatility of material system and shape.[46] In order to effectively use these patterns in device applications, the resulting quantum dot arrays must be regular, uniform, and retain their optical activity.

Focused Ion Beams

The FIB ionizes pure metal into metal ions. Gallium is the primary liquid metal ion source used[47], but alternative ion sources include Au and Ir. The ions are accelerated similarly to electrons in an SEM, and they penetrate the surface. If the dose of the ions is low enough, the sample could be implanted with the ions. If the dose is high enough, it will sputter the surface. In this manner the FIB acts as a chisel and can remove material from a targeted sample. The FIB is used for cross-sectional SEM investigation and for TEM sample preparation. The capability to select the precise TEM sample site has never been available before, but ion damage must be minimized when viewing electron transparent samples. The FIB system also has gas additions that enable platinum deposition, which can be useful in reconnecting leads in device failures.

Commonly used alongside FIB, Stopping and Ranges of Ions in Matter (SRIM) calculations predict penetration depths of ions and reaction cascades in various

materials.[48] The calculations are based on ion interactions with the target material, taking into consideration the density, electronic structure, and bonding. Using SRIM software version 2008.5, we calculated 100,000 ions with 30 kV Ga ions implanted into amorphous GaAs. SRIM calculations show the penetration depth of the ions is 18 ± 10 nm and the lateral movement is 6.5 ± 8.5 nm. Vacancies were shown to penetrate 30 nm into the material.

References

[1] Averett K L, Wu X, Koch M W and Wicks G W. 2003 *J Cryst Growth* **251** 852-857

[2] Yoffe A D. 2001 *Adv Phys* **50** 1-208

[3] Tangring I, Wang S M, Gu Q F, Wei Y Q, Sadeghi M, Larsson A, Zhao Q X, Akram M N and Berggren J. 2005 *Appl Phys Lett* **86** ARTN 171902

[4] Leonard D, Krishnamurthy M, Reaves C M, Denbaars S P and Petroff P M. 1993 *Appl Phys Lett* **63** 3203-3205

[5] Tersoff J, Teichert C and Lagally M G. 1996 *Phys Rev Lett* **76** 1675-1678

[6] Lee H, Johnson J A, He M Y, Speck J S and Petroff P M. 2001 *Appl Phys Lett* **78** 105-107

[7] Suzuki Y, Ohmori Y and Okamoto H. 1986 *J Appl Phys* **59** 3760-3767

[8] Shchukin V A and Bimberg D. 1999 *Rev Mod Phys* **71** 1125-1171

[9] Schmidt O G. *Lateral Alignment of Epitaxial Quantum Dots*. New York: Springer Berling Heidelberg; 2007

[10] Bauer E. 1958 *Z Kristallogr* **110** 372-394

[11] Goldstein L, Glas F, Marzin J Y, Charasse M N and Leroux G. 1985 *Appl Phys Lett* **47** 1099-1101

[12] Leonard D, Pond K and Petroff P M. 1994 *Phys Rev B* **50** 11687-11692

[13] Moison J M, Houzay F, Barthe F, Leprince L, Andre E and Vatel O. 1994 *Appl Phys Lett* **64** 196-198

[14] Ponchet A, Lecorre A, L'Haridon H, Lambert B and Salaun S. 1995 *Appl Phys Lett* **67** 1850-1852

[15] Porte L. 2004 *J Cryst Growth* **273** 136-148

[16] Asaro R J and Tiller W A. 1972 *Metall Trans* **3** 1789

[17] Grinfeld M A. 1986 *Dokl Akad Nauk Sssr* **290** 1358-1363

[18] Srolovitz D J. 1989 *Acta Metall Mater* **37** 621-625

[19] Spencer B J, Voorhees P W and Davis S H. 1993 *J Appl Phys* **73** 4955-4970

[20] Vanderbilt D and Wickham L K. 1991 *Mater Res Soc Symp P* **202** 555-560

[21] Jesson D E, Pennycook S J, Baribeau J M and Houghton D C. 1993 *Phys Rev Lett* **71** 1744-1747

[22] Yang W H and Srolovitz D J. 1993 *Phys Rev Lett* **71** 1593-1596

[23] Vurgaftman I, Meyer J R and Ram-Mohan L R. 2001 *J Appl Phys* **89** 5815-5875

[24] Eberl K, Lipinski M O, Manz Y M, Winter W, Jin-Phillipp N Y and Schmidt O G. 2001 *Physica E* **9** 164-174

[25] Kovsh A R, Maleev N A, Zhukov A E, Mikhrin S S, Vasil'ev A P, Semenova E A *et al*. 2003 *J Cryst Growth* **251** 729-736

[26] Alloing B, Zinoni C, Zwiller V, Li L H, Monat C, Gobet M, Buchs G, Fiore A, Pelucchi E and Kapon E. 2005 *Appl Phys Lett* **86** ARTN 101908

[27] Ward M B, Karimov O Z, Unitt D C, Yuan Z L, See P, Gevaux D G, Shields A J, Atkinson P and Ritchie D A. 2005 *Appl Phys Lett* **86** ARTN 201111

[28] Chu L, Arzberger M, Bohm G and Abstreiter G. 1999 *J Appl Phys* **85** 2355-2362

[29] Henini M, Sanguinetti S, Brusaferri L, Grilli E, Guzzi M, Upward M D, Moriarty P and Beton P H. 1997 *Microelectr J* **28** 933-938

[30] Heitz R, Ramachandran T R, Kalburge A, Xie Q, Mukhametzhanov I, Chen P and Madhukar A. 1997 *Phys Rev Lett* **78** 4071-4074

[31] Tarasov G G, Mazur Y I, Zhuchenko Z Y, Maassdorf A, Nickel D, Tomm J W, Kissel H, Walther C and Masselink W T. 2000 *J Appl Phys* **88** 7162-7170

[32] Liu H Y, Hopkinson M, Harrison C N, Steer M J, Frith R, Sellers I R, Mowbray D J and Skolnick M S. 2003 *J Appl Phys* **93** 2931-2936

[33] Liu G T, Stintz A, Li H, Malloy K J and Lester L F. 1999 *Electron Lett* **35** 1163-1165

[34] Schuh D, Bauer J, Uccelli E, Schulz R, Kress A, Hofbauer F, Finley J J and Abstreiter G. 2005 *Physica E* **26** 72-76

[35] Solomon G S, Trezza J A, Marshall A F and Harris J S, Jr. 1996 *Phys Rev Lett* **76** 952-955

[36] Nakamura Y, Schmidt O G, Jin-Phillipp N Y, Kiravittaya S, Muller C, Eberl K, Grabeldinger H and Schweizer H. 2002 *J Cryst Growth* **242** 339-344

[37] Watanabe S, Pelucchi E, Dwir B, Baier M, Leifer K and Kapon E. 2004 *Physica E* **21** 193-198

[38] Kiravittaya S, Rastelli A and Schmidt O G. 2005 *Appl Phys Lett* **87** ARTN 243112

[39] Taylor C, Marega E, Stach E A, Salamo G, Hussey L, Munoz M and Malshe A. 2008 *Nanotech* **19** ARTN 015301

[40] Vandervelde T E, Atha S, Hull R, Pernell T L and Bean J C. 2006 *J Vac Sci Technol A* **24** 375-381

[41] McKay H A, Dehne A, Lee J Y and Millunchick J M. 2007 *Appl Phys Lett* **90** 163109

[42] McKay H, Rudzinski P, Dehne A and Millunchick J M. 2007 *Nanotech* **18** 455303

[43] Kim Y K, Danner A J, Raftery J J and Choquette K D. 2005 *IEEE J Sel Top Quantum Electron* **11** 1292-1298

[44] Kitslaar P, Strassner M, Sagnes I, Bourhis E, Lafosse X, Ulysse C, David C, Jede R, Bruchhaus L and Gierak J. 2006 *Microelectron Eng* **83** 811-814

[45] Perrey C R, Carter C B, Michael J R, Kotula P G, Stach E A and Radmilovic V R. 2004 *J Microsc* **214** 222-236

[46] Tseng A A. 2004 *J Micromech Microeng* **14** R15-R34

[47] Seliger R L, Ward J W, Wang V and Kubena R L. 1979 *Appl Phys Lett* **34** 310-312

[48] Zeigler J F, Biersack J and Littmark U. *The Stopping and Ranges of Ions in Matter*. New York: Pergamon; 1985

CHAPTER 2 – Experimental Procedures

Great care must be taken in order to successfully reproduce samples. Slight variations in preparation made the surface differ significantly. Small details, such as mounting the sample with a different amount of indium, could lead to uneven heating and a varied starting surface. This section describes the methods used to create and analyze the samples used throughout this study.

Sample Preparation

All of the samples were grown using an EPI 930 solid source molecular beam epitaxy (MBE) on vicinal GaAs(001) or InP(001) substrates with a minimal miscut of 0.1°. Substrates were mounted onto molybdenum scanning tunneling microscope (STM) sample holders with pure indium, and excess indium was removed before insertion into the chamber. The sample composition, deposition rate R_{Ga} and R_{In}, and As flux F_{As} in monolayers per second (ML/s) were calibrated using reflection high-energy electron diffraction (RHEED) oscillations, and the growth temperature T was measured using an optical pyrometer. Arsenic tetramers As_4 were used at a cracking temperature of 600 °C during growth unless otherwise indicated. For Arsenic dimers As_2, the cracking temperature was 1000 °C. Compositions of buffer layers were verified post growth by X-

ray diffraction. At the end of growth, all samples were quenched under an As flux. The samples were then transferred *in vacuo* to the STM for imaging or to the FIB for surface modification. The STM acquired images using a typical sample bias of -3.1 V and tunneling current of 100 pA. The FIB was operated using a 30 kV Ga^+ ion beam and the finest beam resolution achieved was 40 nm at a 10 pA current. Ion beam doses range from 1×10^{15} to 1×10^{18} ions/cm^2. The FIB-treated samples were then put back into the MBE chamber for quantum dot growth and capping. A Digital Instruments Nanoscope IIIa atomic force microscope (AFM) was used to investigate the morphologies of the samples. A JEOL 3011 TEM operating at 300 kV was used to obtain high resolution cross sectional TEM images. Two FIBs were used to create TEM samples: the Quanta 3D and the Nova Nanolab. This procedure is described in more detail later.

FIB Surface Processing

A FEI Magnum ultra high vacuum ion column was outfitted to connect alongside the MBE and STM chambers. A schematic of the multichamber system is shown in Figure 2.1.

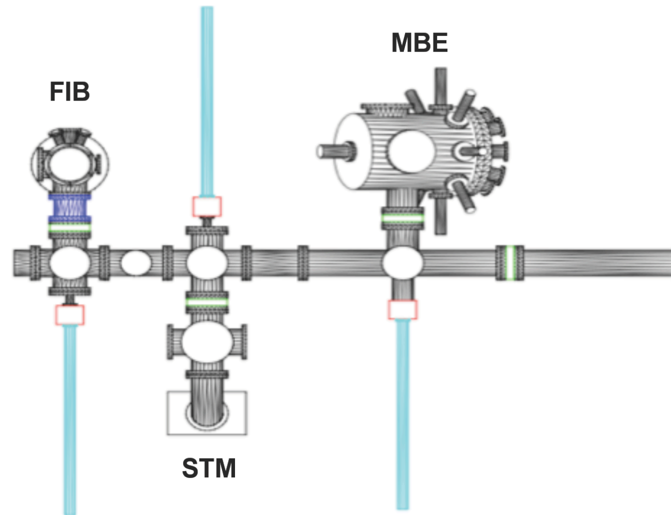

Figure 2.1: Schematic of the combined MBE, STM, and FIB systems.

After the sample was successfully transferred onto the sample stage in the FIB chamber, movement of the stage was controlled by manually adjusting micrometers to pull the sample holder in two directions. The beam had a maximum viewing range of 100 µm to achieve patterning of the finest features allowed by the FIB. Because of this, sample areas were limited to 100 × 100 μm^2. Once that area was irradiated, the stage had to be moved, and thus tiling a single pattern was nearly impossible. Larger sample areas are possible, but minimum feature size will scale up accordingly. Because there was no electron column to assist with focusing, a designated focus area was used and the ion dose in that area was very high. A typical FIB sample would first have designated fiducial marks milled. These fiducial marks consisted of the top half and right half of a square that was approximately 100 µm long and 5 µm thick, and a letter to differentiate the areas. This is shown in Figure 2.2. Then the sample would be divided into four quadrants of approximately 40 µm each. The lower right hand side was used to focus the ion beam, and the other three would be used to pattern with the desired ion dose.

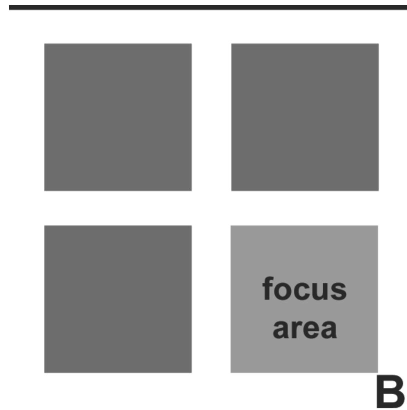

Figure 2.2: Shows a typical FIB-milled sample area that is approximately 100 × 100 μm^2. In this image B is a designation physically milled onto the substrate.

Similarly, *ex situ* FIB used fiducial marks for later identification. These FIB systems had both electron and ion columns, which made focusing much easier. Unnecessary ion beam exposure was minimized because stage movement was automated. The ion beam was focused outside of the area of interest, and then the stage was moved to the correct position for patterning.

FIB for TEM Lift-Out

TEM sample liftout utilized the *ex situ* FIB systems. A layer of platinum was deposited on the sample by first using the electron beam in order to minimize unwanted ion beam exposure in the first 20 nm of the sample. Once the desired area was coated with several hundred nanometers of platinum, ion beam platinum deposition proceeded. Trenches were dug into the sides of the area until a sample of an approximate thickness of 3 μm was left. At this point, a probe was attached to the sample by platinum deposition, and then the sample was freed from the substrate. The probe carried the

sample as it was attached to a copper TEM grid. After this point the sample on the grid was thinned at sequentially lower ion doses to minimize ion damage as the sample reached electron transparency.

Image Analysis

The AFM and STM were used extensively to obtain images, but in order to identify numerical trends, image analysis packages were employed. Wherever possible, scripts were used to speed analysis and mitigate any user bias. The Image Processing Tool Kit in conjunction with Adobe Photoshop, Scanning Probe Image Processing, and DI Nanoscope IIIa AFM software were used to properly threshold and identify features of interest, such as roughness values, step edge density, and feature sizes.

A method used to quantify roughness in an image is to calculate the number of steps within an image. For certain STM images, the step edge density was determined by identifying the step edges at the mid-step heights. The length of those step edges in each image was measured and divided by the total area of the image. First, the images were smoothed. A histogram of the grayscale image was taken, which indicates the different height values associated with the image. Typically, STM images are comprised of various mesas, so the gray level is quantized for each mesa top and is a maxima value in the histogram. The minima between the peaks are associated with the edges. Therefore choosing this pixel color selects these edges as shown in red in Figure 2.3. Then the total line length is measured, and the edge density is calculated.

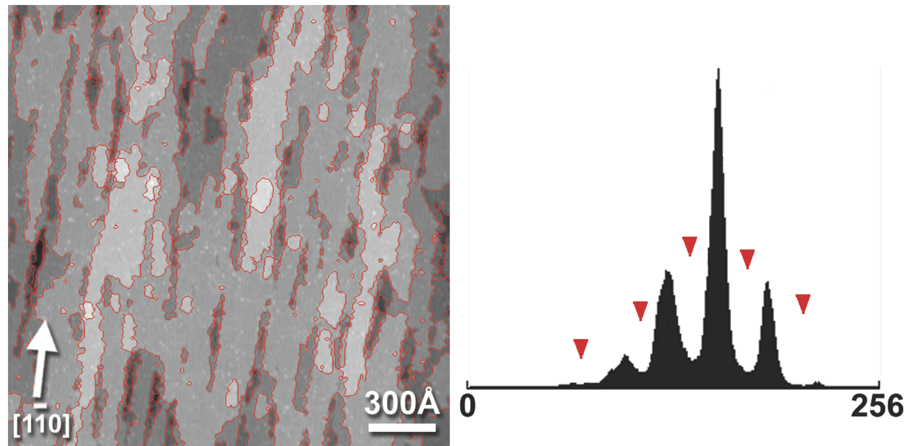

Figure 2.3: A typical scanning tunneling microscopy image of 2 ML GaAs film on $In_{0.53}Ga_{0.47}As$/InP with the edges selected using the histogram on the right.

Photoluminescence Measurements

Two micro photoluminescence (PL) setups were utilized for this study. The first system, called the Ku PL setup (named after the laboratory's principal investigator), consisted of a 532 nm continuous wave pump Nd:YVO_4 laser. PL measurements were made with the sample mounted in a continuous-flow cryostat cooled to 77 K with liquid nitrogen. The laser was focused with a 50× objective lens onto the FIB irradiated regions. A charge-coupled device (CCD) camera verified the location of the laser beam, which had an estimated spot size of 2.6 μm. The PL signal was collected by the same objective lens, analyzed by a 50 cm focal length monochromator, and detected with a liquid nitrogen-cooled InGaAs detector using a lock-in amplifier. An optical filter was placed at the entrance slit of the monochromator to block any backscattered pump light. The power of the laser could be varied from 15-150 mW.

The second PL setup, called the Sih PL setup (named after the laboratory's principal investigator), used either a continuous wave HeNe laser operating at 633 nm

with maximum power of 0.5 mW or a mode-locked Ti:Sapphire laser, which could be tuned from 700-980 nm to achieve a maximum power of 9 mW. The sample was liquid helium cooled to 10 K in a cryostat for measurements. Prior to the laser entering the 100× microscope objective, a fast steering mirror was used to allow spatial scanning across the sample. The beam spot size was estimated to be 1.5 μm and was verified using a CCD camera. The collection path from the sample goes back though the same microscope objective and then through a confocal microscope setup, increasing the signal to noise ratio of the signal. The PL signal is measured on a 75 cm focal length monochromator and detected with a liquid nitrogen-cooled InGaAs detector using a lock-in amplifier. Although the Sih PL setup had a lower laser power, because of the fast steering mirror, it was used more intensely to map out the PL as a function of the scanning location.

CHAPTER 3 – Very Thin Strained Films

These experiments explore how growth parameters can change the morphology of a very thin film. We chose an interesting material system where manipulation of the very initial morphology of 2 ML GaAs is expected to control the shape of further growths of InAs/GaAs short-period superlattices. In this way, we can understand how to change the surface to assemble the mesa-trench structures.

Background

Strain relaxation is present in a phenomenon called lateral composition modulation (LCM). It spontaneously occurs when strained short-period superlattices are formed. Amidst alternating layers in the growth direction, modulations occur in the lateral direction. This modulation could be used for nanowire devices. It has been shown for GaAs/InAs and AlAs/InAs superlattices[1], as well as GaAs/GaSb[2]. At the bottom of the cross-sectional TEM image in Figure 3.1, near the substrate a planar region is visible, where the alternating layers of GaSb and GaAs are first grown. Then a transition region shows where LCM begins. Further from the substrate the LCM continues very strongly.

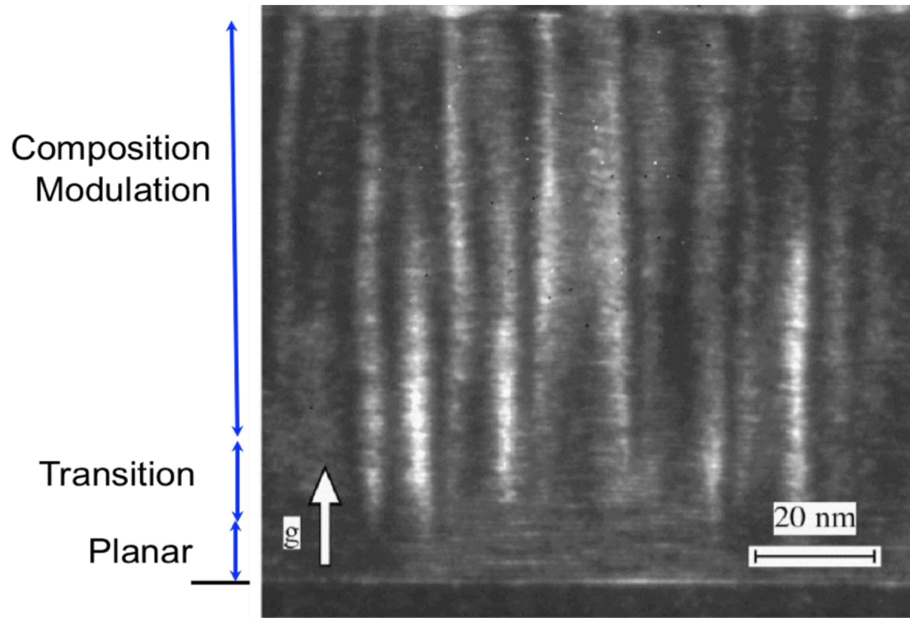

Figure 3.1: Cross-sectional TEM dark field image of lateral composition modulation of a $GaAs_{2ML}$ / $GaSb_{2ML}$ short period superlattice.[3]

STM images were taken of the planar and transition regions, which are shown in Figure 3.2 for the InAs and GaAs short-period superlattice. Figure 3.2 shows the InAs- and GaAs- terminated surfaces for 5, 10, and 15 periods. On the GaAs-terminated surfaces, the terraces in the [110] direction have a correlation length of 150 Å. Because this morphology occurred at the very beginning of 5 periods, it is reasonable to assume that the initial layers quickly dictate the wavelength of the undulations that dominate at higher periods.

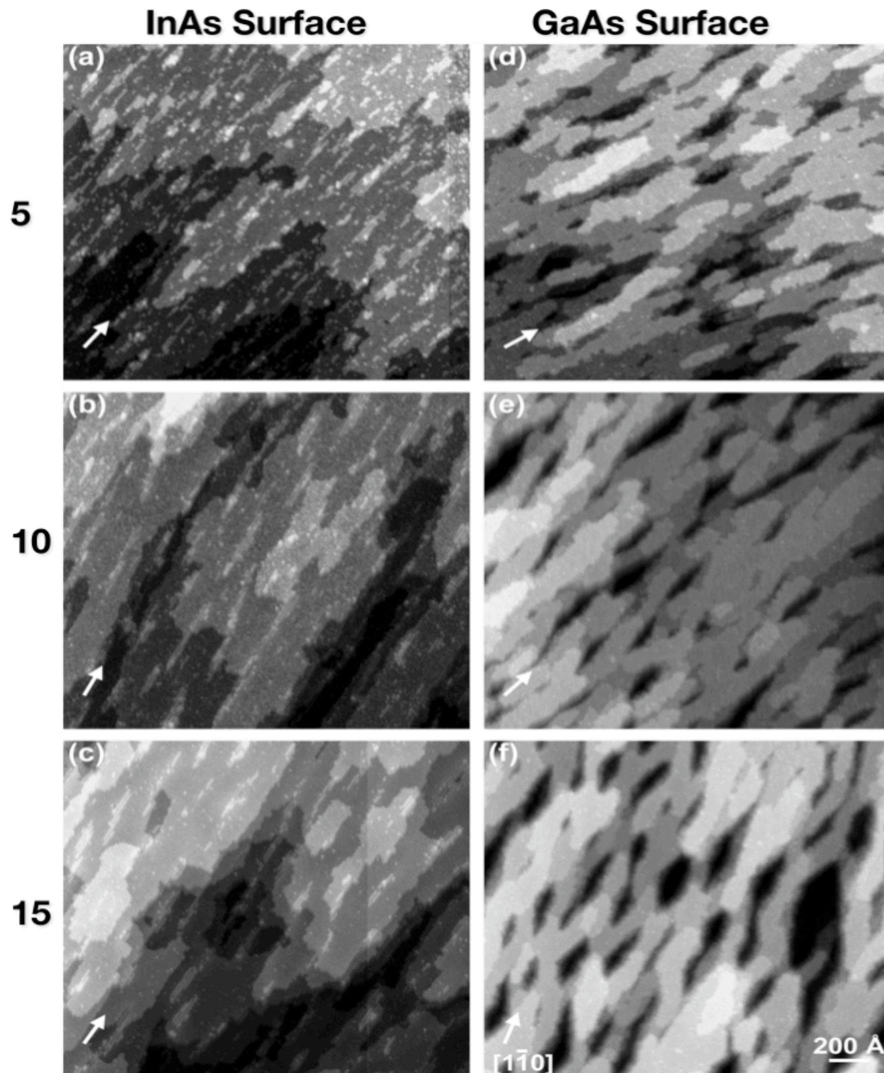

Figure 3.2: STM images of the first 5, 10, and 15 periods of a GaAs/InAs short period superlattice.[4]

For just 2 ML of strained films, the V:III ratio and temperature have been shown to highly affect the morphology of the resulting films. When the V:III ratio decreases or growth temperature increases, films roughen and form facets due to the lack of As on the surface.[5] Also, the diffusivity of adatoms on surfaces is known to depend on the growth conditions.[6-11] Incorporation diffusion lengths have been measured by microprobe RHEED for GaAs homoepitaxy.[6] In these experiments, they have shown

that the diffusion length decreases with increasing As overpressure.[7, 8] Decreasing growth temperature also decreases the diffusion length due to changes in the surface reconstruction.[9] Furthermore, the molecular species of the vapor phase also affects the diffusion length. The use of As_2 during growth reduces the diffusion length compared to the use of As_4.[10, 11]

In this chapter, the morphological evolution of strained thin films is examined. In addition to the mobility of Ga adatoms on the surface, the morphology is greatly affected by the incorporation or disassociation of As. The lattice mismatch strain affects the surface morphology by creating strain-relaxing undulations, thus severely limiting surface diffusion. Despite this, similarities in the morphological evolution akin to homoepitaxial film growth are observed. The results indicate that the morphology is related to the adatom concentration on the surface, which may be predicted by taking into account surface diffusion of Ga adatoms and the reaction of those adatoms with the As overpressure to form GaAs. These results demonstrate the importance of both the group III and more volatile group V fluxes on the morphology of strained films, particularly at low group V fluxes.

Experimental Details

The InP(001) substrates were heated under As overpressure until the oxide layer was desorbed. A 500 nm thick lattice-matched $In_{0.53}Ga_{0.47}As$ buffer layer was grown at T=480 °C, F_{As}=1.5 ML/s and a combined Ga and In growth rate of 0.50 ML/s, which resulted in a smooth (2×4) reconstructed surface according to RHEED and verified by STM as shown in Figure 3.3. The STM image shows terraces running the length of the

200 nm image, having widths of approximately 50 nm. On this smooth buffer layer, 2 ML-thick GaAs films were grown at $0.05 \leq R_{Ga} \leq 0.4$ ML/s, $0.5 \leq F_{As} \leq 5.0$ ML/s and $420 \leq T \leq 540$ °C. The RHEED pattern remained a (2x4) reconstruction during the growth of the tensile strained GaAs films. This procedure has been shown to result in a surface morphology that is planar with occasional two-dimensional islands, having a RHEED pattern that possesses the same reconstruction as during deposition.[4]

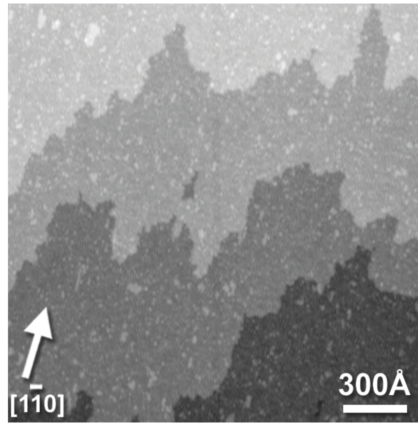

Figure 3.3: STM image of lattice-matched $In_{0.53}Ga_{0.47}As$ buffer layer on InP(001) upon which 2 ML thick GaAs films are grown.

Results

Effect of Ga Growth Rate

Initially, the GaAs films on lattice-matched $In_{0.53}Ga_{0.47}As$ buffer layers samples were grown by keeping the As overpressure constant. STM images are presented in Figure 3.4 of a constant As overpressure (F_{As}=1.5 ML/s), a constant growth temperature of 480 °C, and varying R_{Ga}. Large anisotropic islands are elongated along the [1$\bar{1}$0] direction on the surface. Pits can be seen in all the images, but they seem slightly longer for the higher R_{Ga} of 0.40 ML/s.

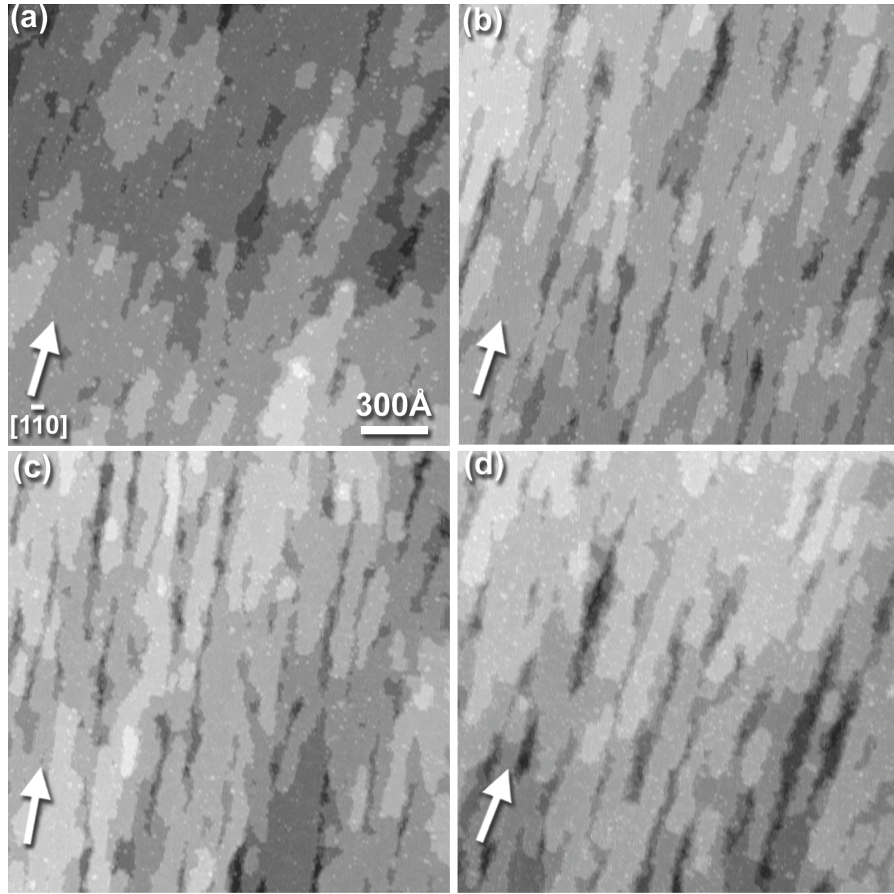

Figure 3.4: STM images of various Ga growth rates for 2 ML of GaAs on InGaAs / InP: R_{Ga}= (a) 0.05, (b) 0.10, (c) 0.20, and (d) 0.40 ML/s with a constant F_{As}=1.5 ML/s.

Effect of Growth Temperature

Changes of the surface morphology with growth temperature are much more apparent in the STM images of GaAs films grown on lattice-matched $In_{0.53}Ga_{0.47}As$ buffer layers at various temperatures are shown in Figure 3.5. The films are grown with R_{Ga}=0.05 ML/s, F_{As}=1.5 ML/s, and temperatures ranging from $420 \leq T \leq 540$ °C. At low temperatures, T=420 °C, large two-dimensional islands elongated along the [1$\bar{1}$0] direction are present on the surface, as shown in Figure 3.5(a). As the growth temperature increases, the island anisotropy and surface roughness also increase. At

intermediate temperatures, T=480 °C, the islands evolve into elongated mesas and pits in the surface, as shown in Figure 3.5(b). At the highest temperatures (T>480 °C), the surface is significantly roughened with very large pits. The STM image of the sample grown at T=540 °C, Figure 3.5(c), shows that the valley-to-peak height exceeds 10 ML, which is greater than the deposited thickness of 2 ML of GaAs. Also, the mesa edges become faceted in the plane of the film, having an angle of 20° away from the $[1\bar{1}0]$, resulting in a zig-zag chain fashion commonly observed in InGaAs/GaAs films.[12-14]

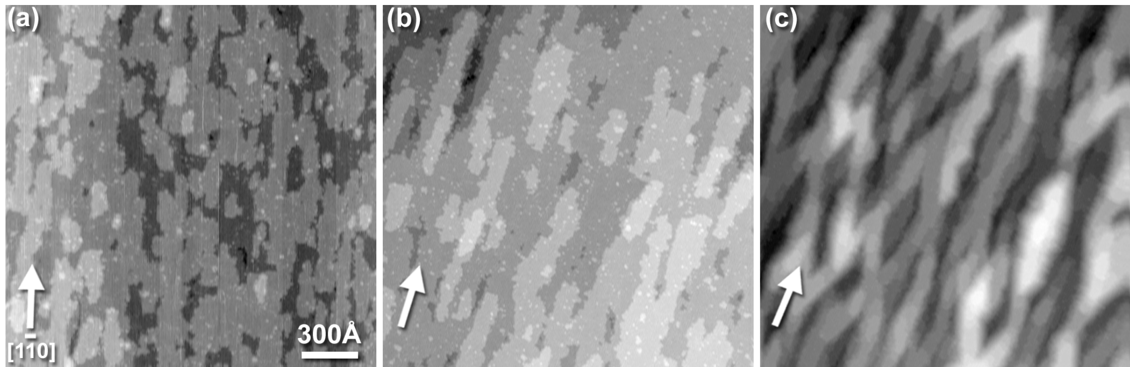

Figure 3.5: Series of STM images for 2 ML thick GaAs films on lattice-matched $In_{0.53}Ga_{0.47}As$/InP grown with R_{Ga}=0.05 ML/s and F_{As}=1.5 ML/s at T= (a) 420, (b) 480, and (c) 540 °C.

In addition to the increase in roughness, the STM images in Figure 3.5 suggest that the elongated mesas take on a characteristic width. The average width was determined by analyzing several line scans from each STM image along the [110] direction. A mesa width was measured as the distance between a distinct beginning and end point within a line scan showing neither interrupting islands nor pits. These average mesa widths are shown in Table 3.1. At low temperatures, the average mesa width obtained using this method is approximately 10 nm with a very large standard deviation of 9 nm. Because the deviation is on the same order as the average width, no single

wavelength of the roughness can be said to exist for these films at these growth conditions. At higher temperatures, the average mesa width decreases to approximately 6 nm with a smaller standard deviation of 3 nm, i.e., the mesas are more uniform in size and a single mesa width is more prominent.

Temperature T (°C)	Average Mesa Width L (nm)
420	9.0 ± 6.2
440	10.1 ± 9.8
450	11.1 ± 9.3
470	10.1 ± 7.1
480	7.8 ± 5.3
510	6.1 ± 2.6
540	5.2 ± 2.8

Table 3.1: Average mesa width determined from STM images for 2 ML thick GaAs films on lattice-matched $In_{0.53}Ga_{0.47}As$/InP grown at various temperatures with R_{Ga}=0.05 ML/s and F_{As}=1.5 ML/s.

It is possible that the increased roughness observed in these films is due to the ATG growth instability. In this case, the undulation wavelength would be expected to depend only on the ratio γ/ε^2, where γ is the surface energy and ε is the lattice mismatch strain.[15-18] As a result, the wavelength is expected to increase with increasing surface energy, or decrease with increasing strain. This model does not have an explicit dependence of the wavelength with temperature. Table 3.1 however, shows that the mesa widths, which are proportional to the undulation wavelength, decrease with growth temperature. This implies that either the lattice mismatch strain increases with

temperature, or that the surface energy decreases. At higher temperatures, intermixing between the buffer layer and the film would be expected to alleviate strain. Such intermixing would be expected to cause the mesa widths to increase in size.[19] Coherent Bragg rod analysis (COBRA) show that films deposited at higher T have more intermixing, thus producing a less strained film.[20] Therefore lattice mismatch strain is not likely a dominant factor in the morphological evolution in these experiments. Instead, the change in mesa width is likely to be the result of a temperature-induced change in the surface energy, perhaps due to desorption of atoms from the surface.

In addition to a change in the mesa width, Figure 3.5 also shows that the films roughen with increasing temperature. In order to quantify the roughness, the step edge density was determined and shown in Figure 3.6. The points of the Arrhenius plot of Figure 3.6 are the log of the step edge densities N (nm^{-1}) as a function of T^{-1} for R_{Ga}=0.2 and R_{Ga}=0.05 ML/s and F_{As}=1.5 ML/s. At low temperatures the step edge density is nominally constant for both growth rates with the step edge density slightly higher for R_{Ga}=0.2 ML/s. This behavior is expected; higher growth rates yield higher nucleation rates and shorter diffusion lengths, resulting in rougher surfaces. At T>500 °C, however, there is a rapid rise in the step edge density at high temperature regardless of R_{Ga}.

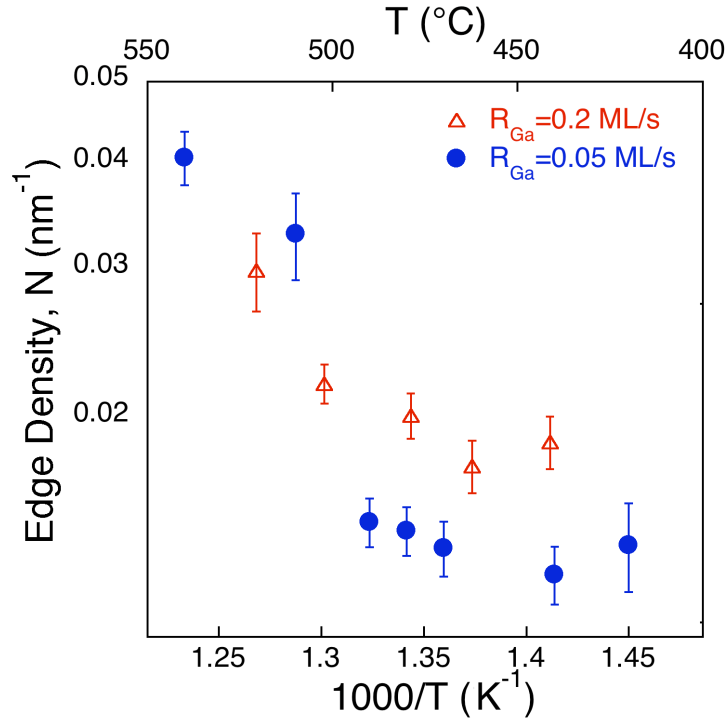

Figure 3.6: Arrhenius plot of the edge densities *N* as a function of inverse *T* for 2 ML thick GaAs films on lattice-matched $In_{0.53}Ga_{0.47}As/InP$ deposited with F_{As}=1.5 ML/s at R_{Ga}=0.2 ML/s and R_{Ga}=0.05 ML/s.

The increase in step edge density with temperature may be due to a number of factors. At low growth temperatures, step edge attachment is essentially irreversible; once an adatom is attached to a step edge, the activation energy for detachment is so great that the likelihood of the adatom leaving the step edge is very low.[21] However, at high temperatures, the likelihood of adatom detachment is non-negligible. Accordingly, the morphology would be rougher at lower temperatures because of the lack of detachment and smoother at higher temperatures because rearrangement is possible.

Intermixing: COBRA Results

Further examination of the top few monolayers was conducted by using COBRA.[20] This x-ray technique is useful because it is nondestructive and can be used to study buried structures and interfaces. It combines the energy dependence of the atomic scattering factor and subangstrom resolution of the atomic species. This approach gives details about the composition and strain profiles of the two samples shown in Figure 3.7, one grown at 480 °C and the other at 520 °C.

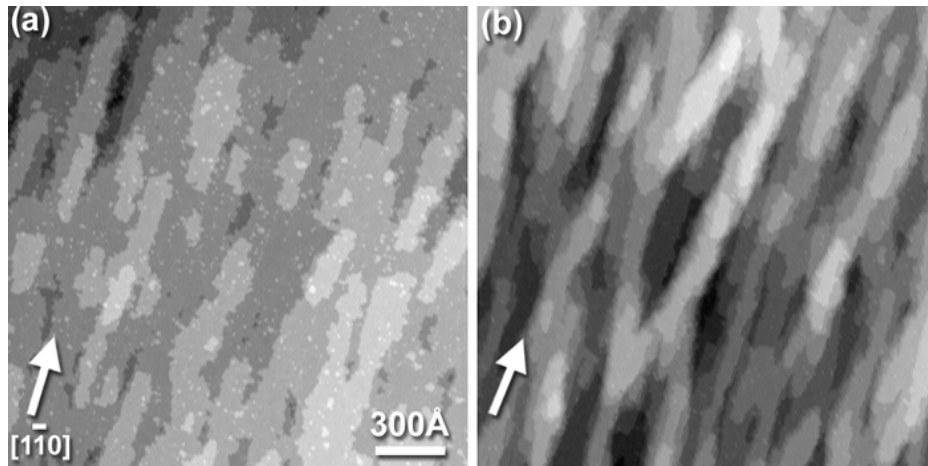

Figure 3.7: STM images of 2 ML GaAs films on lattice-matched $In_{0.53}Ga_{0.47}As$/InP grown at T = (a) 480 °C and (b) 520 °C.

Complex scattering factors are collected from the Bragg rods to help produce electron density distributions. Then the fractional occupancies f_z are calculated and fit to the samples, which matched up very closely to the histogram of heights as seen in Figure 3.8. There was very little intermixing between the group III and group V lattice sites, indicating that there were not many defects in the crystal structure. The f_z values help to indicate where the As sites are vacant and they corroborate the height profiles. Once these sites have been identified, this can then be used to further calculate the In content at

the various levels and the % in-plane strain in Figure 3.9. The results verified the buffer layer to be $In_{0.53}Ga_{0.47}As$. Near the buffer-film interface both samples had an In content of approximately 40%, and at the surface there was about 20% In. Using this method the amount of In desorbed at the buffer can be calculated to be 0.03 ML for 480 °C and 0.2 ML at 520 °C. The strain was calculated by using the Poisson ratio and measuring the composition and out-of-plane lattice spacing. Both tensile films have a strong strain component, but the 520 °C has more strain compensation with lower strain at the surface than the 480 °C sample. The In incorporation from the buffer layer reduces the strain by expanding the lattice. This confirms that more relaxation at the higher temperature is observed in surface roughening. If we compare the COBRA strain results with the mesa widths, we see that the strain energy γ decreased by approximately 50% at the higher temperature, most likely from the desorption of adatoms.

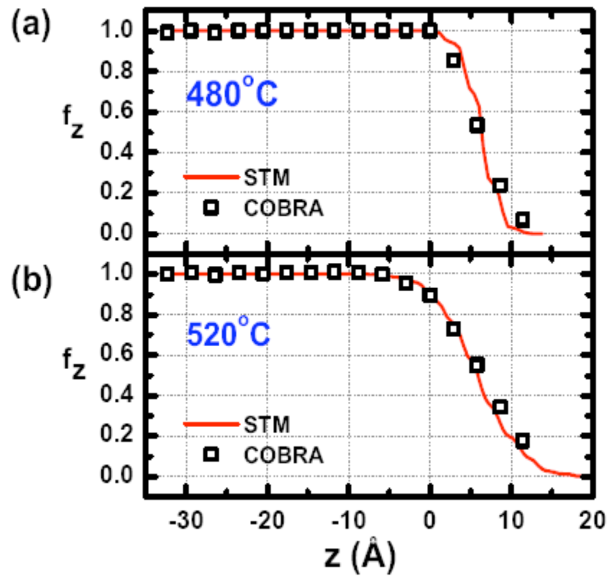

Figure 3.8: COBRA occupancy profiles align closely with STM height profiles of samples grown at (a) 480 °C and (b) 520 °C.[20]

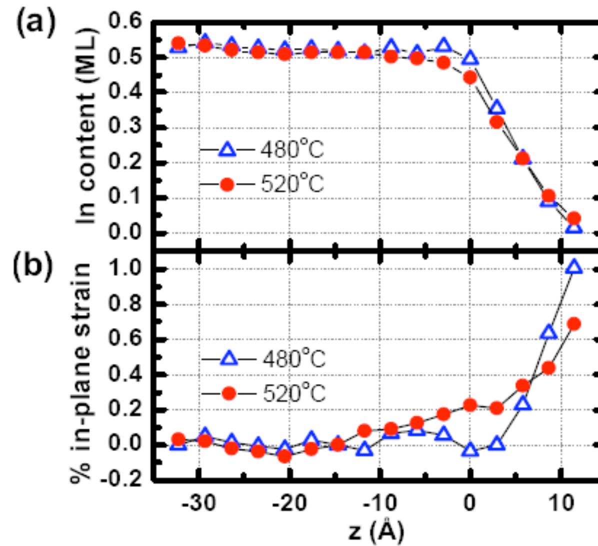

Figure 3.9: COBRA results of (a) In content and (b) strain as a function of the distance from the top most layers.[20]

Mathematical Model

It is well known that As has a higher vapor pressure compared to GaAs at typical growth temperatures. The overpressure creates an abundance of As and is necessary to maintain stoichiometry of the film. As the As desorbs from the surface at high temperatures, there is an increase in the Ga adatom population and thus the roughness, as shown both computationally[22, 23] and experimentally[24, 25]. Detailed kinetic Monte Carlo (KMC) simulations for GaAs surfaces over a large range in temperature have shown that there is a temperature at which the rate of island nucleation is at a minimum, and above and below that temperature, the island nucleation rate increases rapidly. In these calculations, As desorption causes a rise in the nucleation rate at high temperatures[22] resulting in roughened growth morphologies at higher temperatures (T>530 °C). A roughening transition at T=510 °C has been observed experimentally for

homoepitaxial GaAs films.[25] Our results for tensile GaAs films deposited on $In_{0.53}Ga_{0.47}As/InP$ show a similar transition, however at a somewhat lower temperature of $T \approx 500$ °C. This transition is independent of R_{Ga} as it can be seen at both growth rates in Figure 3.6.

A model that includes both the diffusion of group III and incorporation of group V atoms from the vapor may be used to explain the morphological evolution of these films. The Ga adatom density η_{Ga}, which affects the nucleation rate and thus the morphology of the film, was shown by Orr et al[23] to be given by:

$$\eta_{Ga} = \frac{R_{Ga}L^2}{2D_0 \exp\frac{-E_d}{kT}} + \nu_{Ga}\left(\frac{F_{As}}{F_{As0}}\right)^{-1/m} \exp\frac{-E_x}{kT} \quad \textbf{(1)}$$

The first term accounts for the Ga adatom diffusion on the surface, the Ga growth rate, R_{Ga}, and the distance between steps, L. It is important to note that in these experiments L, the mesa length, is set by the ratio of the surface energy and lattice mismatch strain, and is not necessarily related to the diffusion length of adatoms on the surface. As T increases, the diffusion term acts to reduce the adatom concentration. The second term takes into account the reduction of Ga adatoms on the surface due to their reaction with As to form immobile GaAs. This term has an Arrhenius dependence, where E_x is the binding energy of GaAs. The prefactor terms include the density of available surface sites for Ga, ν_{Ga}, and the flux of As, where m is the number of As atoms in the vapor molecule (in these experiments m=4 unless otherwise specified). As the temperature increases, As desorbs from the surface, releasing Ga adatoms. As T decreases, more As react with Ga adatoms, thus reducing their population. For systems where the binding energy is much greater than the diffusion energy (E_x>>E_d), the second term is negligible,

and η_{Ga} is dominated by diffusion. Under these conditions, desorption from the surface is minimal, and the film roughens at very low temperatures since there is not enough energy for the adatoms to diffuse. An example of this can be found in the Si and SiGe systems, where the high binding energies minimize the effects of desorption.[26] When the binding energy is much smaller than the diffusion energy ($E_x \ll E_d$), desorption from the surface controls adatom density. When the binding energy and diffusion energy are similar ($E_x \approx E_d$), the two terms compete. Under these conditions diffusion dominates the adatom concentration at low temperatures, and desorption dominates at high temperatures, as seen in homoepitaxial growth of GaAs.[25]

Samples analyzed in this study were rapidly quenched from the growth temperature, preserving the growth morphology. Adatoms present during growth are captured by step edges, or nucleate new mesas upon quenching. Therefore it is reasonable to assume that η_{Ga} is directly related to the step edge density N. Figure 3.6 shows experimentally determined values of step edge density N fit to Equation (1) using accepted values for Ga diffusion energy of E_d=1.5 eV[27], the binding energy of GaAs E_x=1.73 eV[28], and the average measured mesa length taken from Table 3.1 (L=8 nm), along with the experimental parameters F_{As}, R_{Ga}, and T. Figure 3.10 shows the theoretical values for the Ga adatom density η_{Ga} are in excellent agreement with the experimental step edge density data N, confirming the assumption that η_{Ga} is proportional to N.

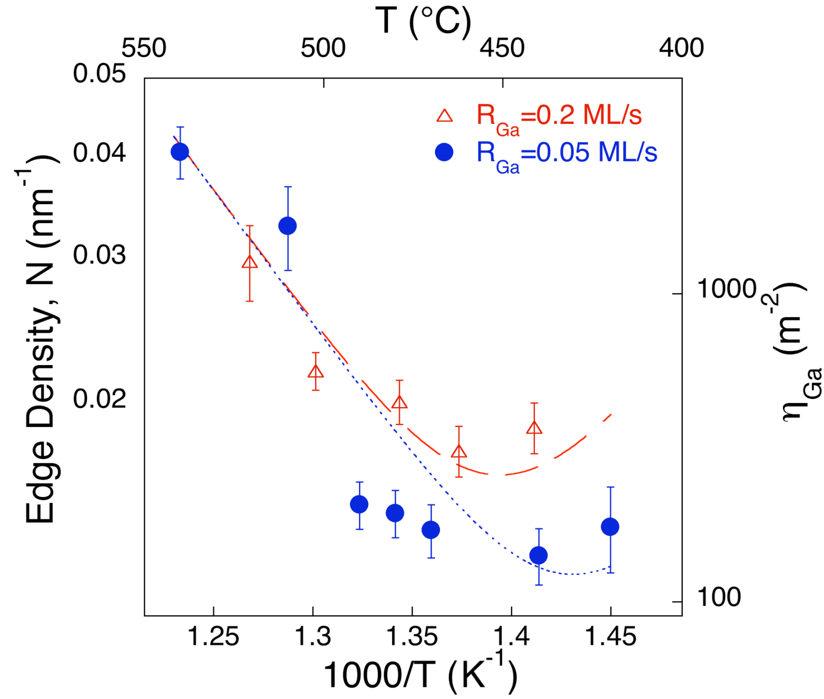

Figure 3.10: Arrhenius plot of the edge densities *N* as a function of inverse *T* for 2 ML GaAs films on lattice-matched $In_{0.53}Ga_{0.47}As$/InP deposited with F_{As}=1.5 ML/s at R_{Ga}=0.2 ML/s and R_{Ga}=0.05 ML/s. Calculated Ga adatom densities η_{Ga} are shown as lines (dotted for R_{Ga}=0.05 ML/s and dashed for R_{Ga}=0.2 ML/s).

Effect of As Overpressure

The form of Equation (1) shows that the relationship between the growth rate, R_{Ga}, and the As flux, F_{As}, is not linear. Instead, η_{Ga} and thus the surface morphology are more sensitive to F_{As}, which has a $-1/m$ dependence, than R_{Ga}, which has a linear dependence. This is verified by our experiments. Figure 3.11 shows the step edge densities of films grown at constant temperature and varying R_{Ga} or F_{As}. With decreasing F_{As} and increasing R_{Ga}, *N* increases and the films roughen regardless of the values of F_{As} and R_{Ga}. However low F_{As} has a stronger effect than high R_{Ga} on the amount of

roughening incurred. This is shown in the STM images in Figure 3.11(b) and (c), which have the same F_{As}:R_{Ga} ratio of 15:1, but different absolute fluxes and growth rates. N is lower for the higher absolute flux of F_{As} and R_{Ga} of 1.5 and 0.1 ML/s respectively.

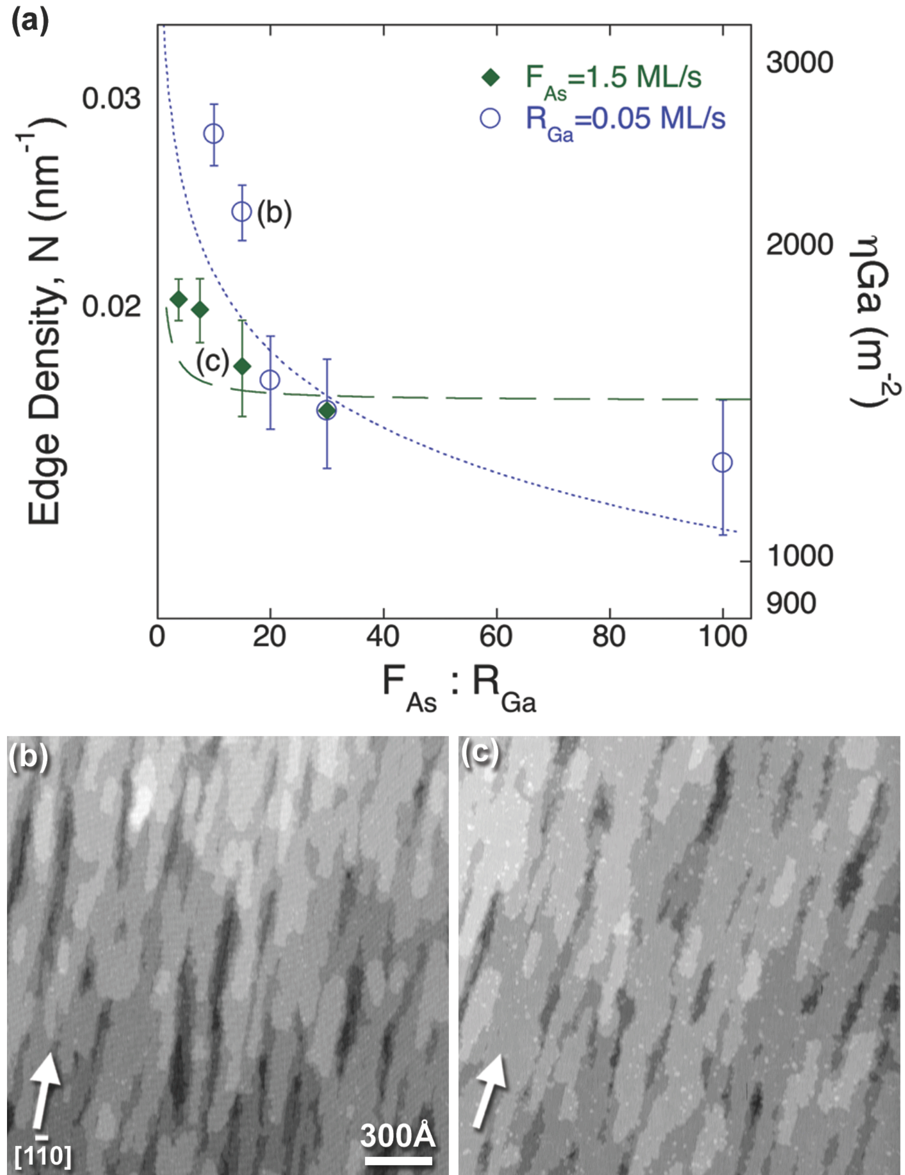

Figure 3.11: (a) Plot of the edge densities N as a function of F_{As}:R_{Ga} for 2 ML thick GaAs films on lattice-matched $In_{0.53}Ga_{0.47}As$/InP deposited at T=480 °C. Calculated Ga adatom densities η_{Ga} are shown as lines (dotted for R_{Ga}=0.05 ML/s and dashed for F_{As}=1.5 ML/s). Representative STM images are shown for the growth conditions such that the F_{As}:R_{Ga} ratio of 15:1 is the same: (b) was grown with R_{Ga}=0.05 ML/s and F_{As}=0.75 ML/s, and (c) was grown with R_{Ga}=0.1 ML/s and F_{As}=1.5 ML/s.

If As_2 dimers are used instead of As_4 tetramers, Equation (1) predicts that the films will have a lower Ga adatom density, and thus be smoother. In order to test this, two films were grown under the same conditions (T=520 °C, R_{Ga}=0.05 ML/s, F_{As}=1.0 ML/s) but with varied As species: As_2 dimers and As_4 tetramers. RHEED patterns of the films indicate that both films have the same (2×4) reconstruction during growth, but upon cooling the RHEED pattern for the As_4-grown film becomes a slightly modulated (2×1) reconstruction, while the RHEED pattern for the As_2-grown film becomes spotty with distinct chevrons. Figure 3.12 shows the STM images of the two grown films. The surface of the tetramer-grown sample has an undulating appearance, while the surface of the dimer-grown sample has mesas with more narrow trenches. The film roughness and edge densities in these films are similar. The adatom concentration may not be the only factor influencing the morphologies of As_4- and As_2-grown films. It is likely that the details of the surface reconstruction, the incorporation of the As, and thus the surface energy of these films, are the dominant drivers of the morphological evolution for films grown under As_2 versus As_4.[10, 29]

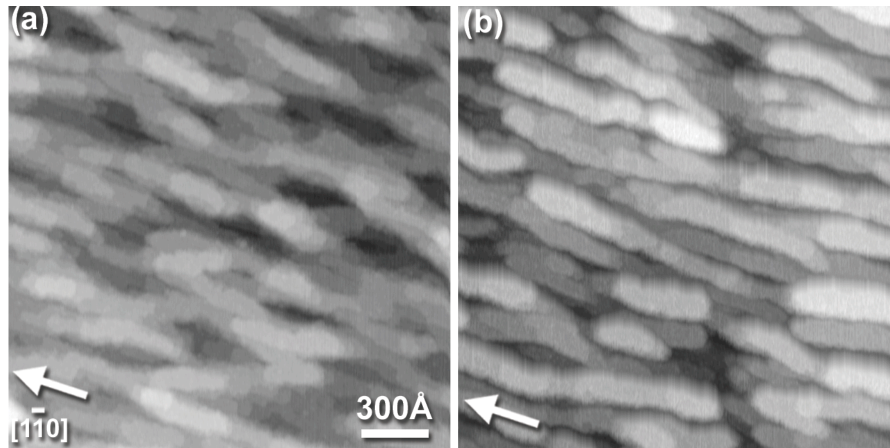

Figure 3.12: STM images for 2 ML thick GaAs films on lattice-matched $In_{0.53}Ga_{0.47}As$/InP grown with R_{Ga} of 0.05 ML/s at T= 520 °C and F_{As} of 1.0 ML/s, and with (a) As tetramers, As_4, and (b) As dimers As_2.

Conclusions

Using *in vacuo* STM, we have imaged 2 ML GaAs films grown on lattice-matched $In_{0.53}Ga_{0.47}As$/InP(001). The films possess mesa-trench morphology, and we observed the mesa width decreased with increasing growth temperature. At higher growth temperatures intermixing reduced the lattice mismatch strain of the film. While the ATG instability model does not have explicit temperature dependence, it would predict an increase in mesa length from the reduction of lattice mismatch strain, which is in contrast to our results. COBRA results confirmed the presence of In on the surface of the film at high growth temperatures, allowing for strain relaxation within the film. Thus, the decrease in mesa width is likely the result of temperature dependence of the surface energy, which decreased by 50%. Comparison of the experimental data to a Ga adatom density model that accounts for both the diffusion of group III atoms and the incorporation of group V atoms from the vapor demonstrates excellent agreement. Our

observations show that, in contrast to common practice, the V:III deposition ratio is not an appropriate growth parameter because the dependence of the morphology on F_{As} is stronger than on R_{Ga}. There is a lower limit for As overpressure at which the rate of As increases the film roughness. Films grown with As_4 or As_2 show similar roughness, indicating that the species in the vapor phase has a strong effect on the surface energy of the films.

References

[1] Dorin C and Millunchick J M. 2002 *J Appl Phys* **91** 237-244

[2] Dorin C, Mirecki Millunchick J and Wauchope C. 2003 *J Appl Phys* **94** 1667-1675

[3] Dorin C, Millunchick J M and Wauchope C. 2002 *Appl Phys Lett* **81** 3368-3370

[4] Pearson C, Dorin C, Millunchick J M and Orr B G. 2004 *Phys Rev Lett* **92** 056101

[5] Tok E S, Neave J H, Fahy M R, Allegretti F E, Zhang J, Jones T S and Joyce B A. 1997 *Microelectr J* **28** 833-839

[6] Hata M, Isu T, Watanabe A and Katayama Y. 1990 *J Vac Sci Technol B* **8** 692-696

[7] Yamashiki A and Nishinaga T. 1999 *J Cryst Growth* **198** 1125-1129

[8] Nishinaga T, Shen X Q and Kishimoto D. 1996 *J Cryst Growth* **163** 60-66

[9] Lopez M and Nomura Y. 1995 *J Cryst Growth* **150** 68-72

[10] Ogura T and Nishinaga T. 2000 *J Cryst Growth* **211** 416-420

[11] Sugaya T, Nakagawa T, Sugiyama Y, Tanuma Y and Yonei K. 1997 *Jpn J Appl Phys 1* **36** 5670-5673

[12] Porte L. 2004 *J Cryst Growth* **273** 136-148

[13] Krapf P, Robach Y, Gendry M and Porte L. 1997 *J Cryst Growth* **181** 337-342

[14] Chokshi N S and Millunchick J M. 2000 *Appl Phys Lett* **76** 2382-2384

[15] Asaro R J and Tiller W A. 1972 *Metall Trans* **3** 1789

[16] Grinfeld M A. 1986 *Dokl Akad Nauk Sssr* **290** 1358-1363

[17] Srolovitz D J. 1989 *Acta Metall Mater* **37** 621-625

[18] Spencer B J, Voorhees P W and Davis S H. 1993 *J Appl Phys* **73** 4955-4970

[19] Sowwan M, Yacoby Y, Pitney J, MacHarrie R, Hong M, Cross J, Walko D A, Clarke R, Pindak R and Stern E A. 2002 *Phys Rev B* **66** ARTN 205311

[20] Kumah D P, Riposan A, Cionca C N, Husseini N S, Clarke R, Lee J Y, Millunchick J M, Yacoby Y, Schleputz C M, Bjork M and Willmott P R. 2008 *Appl Phys Lett* **93** ARTN 081910

[21] Tromp R M and Hannon J B. 2002 *Surf Rev Lett* **9** 1565-1593

[22] Kratzer P, Penev E and Scheffler M. 2002 *Appl Phys A-Mater* **75** 79-88

[23] Tersoff J, Johnson M D and Orr B G. 1997 *Phys Rev Lett* **78** 282-285

[24] Ding Z, Bullock D W, Thibado P M, LaBella V P and Mullen K. 2003 *Phys Rev Lett* **90** ARTN 216109

[25] Riposan A, Martin G K M, Bouville M, Falk M L and Millunchick J M. 2003 *Surf Sci* **525** 222-228

[26] Hubbard K J and Schlom D G. 1996 *J Mater Res* **11** 2757-2776

[27] Yang H, LaBella V P, Bullock D W, Ding Z, Smathers J B and Thibado P M. 1999 *J Cryst Growth* **201** 88-92

[28] Chatillon C, Ansara I, Watson A and Argent B B. 1990 *Calphad* **14** 203-214

[29] Holmes D M, Belk J G, Sudijono J L, Neave J H, Jones T S and Joyce B A. 1995 *Appl Phys Lett* **67** 2848-2850

CHAPTER 4 – FIB-Induced InAs Quantum Dots

Ultimately the goal of this material system is to produce reliably sized, uniform InAs quantum dots on GaAs for the best device performance. There is a push for optoelectronic devices to move from quantum wells to quantum wires to quantum dots to achieve the most efficiency of material and smallest dimensions. In order to do that we must first characterize the size and number of quantum dots that form for different growth conditions and patterns. We would like to understand the growth mechanisms of the quantum dot so we could better understand the precise placement of the dots. This chapter focuses mainly on the effect of FIB patterning of GaAs to alter the shape of InAs quantum dots both computationally and experimentally.

The surface patterns consist of milled holes in the GaAs substrate or buffer layer. First a computational model is proposed employing KMC simulations of the growth that include elastic relaxation of the lattice to show that the location, size, and number of dots can be delicately tuned by controlling growth conditions and hole geometry. Second, we connect physical experiments to our computation models to verify our understanding of the impact of FIB patterning on the growth of quantum dots. We conduct both *ex situ* and *in vacuo* FIB patterning. In the former we find that the oxide layer is an obstacle in creating a smooth starting surface, and consequently our *ex situ* FIB laboratory setup is shown to be an inefficient method for creating quantum dots. The remainder of this

chapter uses *in vacuo* experiments, to examine growth parameters, such as ion dose, thickness, and temperature, along with the periodicity and geometry of the created hole arrays. Finally, we compare our experimental films, studied with AFM, to our calculated structures provided by KMC simulation with elastic contributions from the buffer layer. We find that size, fidelity, and the number of dots are strongly influenced by the FIB-irradiated dwell time. At low ion doses, holes are not always present, but increasing the ion dose increases the fidelity and also enlarges the holes. Multiple dots nucleate around a single hole when the temperature is decreased and when the hole surface area increases. These experiments, along with our numerical model, show that the regularity of the resulting quantum dot arrays is strongly dictated by the initial pattern of holes. Examination of the progression of incremental additions of InAs elucidates the growth mechanisms of the quantum dots.

Background

Simulations of III-V Growths

Computer simulations exist for many different scales, from continuum models that can span millimeters to density functional theory that looks at atoms on the angstrom level. It is convenient to explore experimental results while carefully controlling a single variable at a time. In crystal growth processes, KMC simulations have emerged as useful tools for analysis of growth evolution.[1] Recent KMC simulations have been used as models for different features in III-V semiconductor growth, such as islands[2, 3], step edges[4], and quantum dot formation[5]. The KMC calculation employs a random walk of an atom at discrete locations on the surface. After each random movement, the system

evaluates the dynamics of that choice, and then denies or accepts the movement. By using these types of simulations, we can investigate the evolution of surface morphology, especially in the case of InAs quantum dots on a patterned surface.

Substrate Oxide Desorption

In this chapter we examine patterned surfaces to induce quantum dot growth. With any sample growth, the substrate must first have its oxide layer desorbed in order to have single crystalline growth. There are three main methods of oxide desorption for GaAs: 1) thermal, 2) H-assisted, and 3) Ga-assisted. Thermal desorption is the fastest method and most commonly used in our laboratory. The oxide uses Ga from the bulk to create volatile Ga_2O in this chemical reaction[6, 7]:

$$Ga_2O_3 + 4GaAs \rightarrow 3Ga_2O\uparrow + 2As_2 \text{ (or } As_4)\uparrow$$

The substrate is heated to 610 °C with arsenic overpressure and leads to very rough pitted surfaces.[8] Typically a very thick buffer layer is grown to planarize the surface. This presents a problem when the surface is patterned because a thick buffer layer would obscure the pattern or if left rough, pits become nucleation sites for adatoms.

Hydrogen-assisted desorption occurs by this reaction[9]:

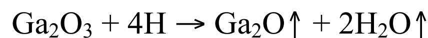

$$Ga_2O_3 + 4H \rightarrow Ga_2O\uparrow + 2H_2O\uparrow$$

The sample is exposed to hydrogen flux at 400-500 °C. The hydrogen can be introduced by thermally cracked hydrogen from passing hydrogen gas over a heated tungsten filament or by rf generated hydrogen plasma sources where the hydrogen is dissociated by rf power.[10] When using this method, one must be careful to not introduce contaminants[11] and not degrade the surface[9]. H-assisted desorption has

been used successfully for electron beam lithographic and nanoimprint lithographic GaAs surfaces, and the patterns remained mostly intact.[10, 12]

Gallium-assisted desorption has been shown to smooth the oxide surface by providing Ga that would otherwise be taken from the bulk[7, 13]:

$Ga_2O_3 + 4Ga \rightarrow 3Ga_2O\uparrow$

This method is easier to implement during growth because there is no additional equipment necessary, such as a hydrogen source. But this method is also very sensitive to the correct amount of Ga introduced for the thickness of the oxide.[13] If excess Ga is introduced, the patterns will fill with the excess material.[10]

Formation of Quantum Dots

Whether patterning *ex situ* or *in situ*, quantum dots have been directed at specific locations in many different material systems. Most methods involve a physical change in the geometry of the surface to begin nucleation of dots at divots.

Ex Situ *Methods*

An *ex situ* method used mechanical deformation to change the surface geometry: Taylor et al created patterns of 40-130 nm wide, 4-760 nm, 1 μm apart nanoindents.[14] They were thermally desorbed, and 28 nm GaAs buffer was grown. Then 2 ML InAs was deposited at 520 °C to form 30-60 nm high, 250-400 nm wide dots, which are massive dots. Also, it is limited by the size and spacing of the nanoindenters. This is an example of a rather large patterning method, but in contrast, STM was used to create very

small holes, 11 nm wide and 3 nm deep in AlInAs surfaces.[15] The STM used a large bias of -8 V and a current of 1 nA, but this method is quite cumbersome to execute.

Patterning techniques include AFM probe lithography[16, 17], interferometric lithography[18], and nanoimprint lithography[12, 19]. Compared to these techniques, electron beam lithography is more versatile because it bypasses the need for a template. Instead the electron beam is used to create complex patterns. Schneider et al used electron beam lithography to manufacture 50 nm wide dots, which is on the finer side of directed InAs quantum dot growth.[20]

Another group that studied electron beam lithography very thoroughly is Atkinson et al.[10] They created holes 0.5-10 μm apart in GaAs. They tried both H-assisted and Ga-assisted desorption that varied the initial pattern slightly to 110 nm wide, 20 nm deep holes. After 8 nm GaAs buffer was deposited, 1.4 ML InAs was grown at 510 °C to form 55 nm wide, 5 nm high dots. During the 8 nm GaAs buffer growth, the holes elongated in the [110] direction to make figure of eight shaped holes because of growth on preferred facets. The resulting holes had 60% instances of double quantum dots and 40% single quantum dots at a single hole site.

The FIB is a promising new method similar to electron beam lithography, but it can be used in a variety of material types and can achieve even smaller feature sizes than electron beam lithography. Some groups use the FIB as a subtractive process to obtain metallic droplets. Lugstein et al FIB irradiated GaAs to leave Ga droplets and also InAs to leave In droplets.[21]

Others use the FIB to make templates of holes for dot nucleation. It has already been used for assembly in other material systems: ZnO dots on Si[22], VO_2 on Si [23], AlInAs[15], Cu_2O on $SrTiO_3$[24], and SiGe on Si[25, 26].

Gray et al grew SiGe quantum dot molecules on *ex situ* FIB-patterned Si substrates. The $Si_{0.7}Ge_{0.3}$ dots were highly faceted square shapes around the hole. At lower ion doses and lower growth temperatures, Karmous et al showed that single Ge dots were placed in the center of the holes instead of quantum dot molecules surrounding the hole. At lower growth temperatures the Ge dots formed in the holes, and at higher temperatures the dots grew around the edges of the holes. They conjecture that at low temperatures the dots form by kinetically limited nucleation and at high temperatures the system is stress-driven nucleation.

In Situ *Methods*

All the *ex situ* methods listed above offer a range of flexibility in processing. However, *in situ* processing allows the grower to not worry about oxide desorption. Without this extra variable, pattern features have one less calibration to deal with. Yokota et al used an *in situ* RHEED to create very wide pits 2 μm across and 8 nm deep.[27] PL results indicate preferred nucleation at these sites, but the hole size is rather large. A finer pattern of holes was created in ultra high vacuum by Ishikawa et al.[28]. They used electron beam lithography to make holes 1.5-5 nm deep, 100 nm wide, and 500 nm apart. A 10-20 nm GaAs buffer layer was grown before 1.8 ML InAs was deposited at 460-490 °C. The step edges from deeper holes yielded more dots, e.g. at 5 nm depth there were 15-25 dots at a single site and at 1.5 nm depth, 1-2 dots were at a

hole. They correlate the depth with the number of InAs quantum dots and assert that atomic steps act as barriers to In migration causing formation of dots where large steps are present.

Mehta et al used *in vacuo* FIB irradiation of GaAs buffer to create FIB-irradiated holes 63 nm wide and 1 μm apart.[29] A re-evaporation step was included to remove any implantation damage from the ion beam. Many different annealing and re-evaporation scenarios were tested and the one that the authors deemed the best results was when the sample was heated to 760 °C and 3-5 nm of GaAs was deposited. InAs quantum dots were grown at 525 °C with 1.4-2.1 ML, and showed 50 quantum dots per FIB spot spanning an area of $300 \times 500\ nm^2$. They achieved 52% single dot occupancy when their growth is fully optimized. If annealed hotter and more GaAs grown, the InAs quantum dots became very spread apart. They conjecture that the holes create sites with lower chemical potential and drive In diffusion to lower the critical thickness for dot formation. When more ions are deposited the hole geometry change results in an increased change in chemical potential, resulting in more quantum dots.

In all the patterning methods reviewed, there are common steps in the experimental procedure and common results: 1) if there is an oxide layer, it must be desorbed carefully so as to not alter the pattern, 2) usually after oxide desorption, there is a small buffer layer grown and sometimes annealing before the dots are deposited, and 3) the hole shape and growth temperature affects whether single or multiple dots form. For the last point, we turn to computer simulations to help us understand how nucleation begins.

Kinetic Monte Carlo Simulations

We have discussed many ways to pattern surfaces for quantum dot formation. In order to investigate the mechanisms of nucleation in response to these patterned arrays of holes, we use a KMC model of crystal growth that take elastic relaxation of the lattice into account. We use a simple solid-on-solid model[30-33] without surface reconstructions and assume that the migrating surface adatoms are units of GaAs or InAs. In other words, we do not take the effect of As overpressure into account. In this model only surface atoms can move and the hopping rate associated with the *p*th surface atom is denoted as r_p. The hopping rate is modeled as

$$r_p = r_0 \exp\left[(-E_d - E + \Delta W)/k_B T\right]$$

where E_d is the diffusion barrier for InAs on GaAs, k_BT is the thermal energy, r_0 is the attempt frequency, and E is the composite bonding energy term given by:

$$E = N_{GG}\, g_{GG} + N_{IG}\, g_{IG} + N_{II}\, g_{II} - 5g_{IG},$$

N_{GG} is the total number of GaAs-GaAs bonds between atom p and its nearest and next nearest neighbors and the bond energy is denoted as g_{GG} . The quantities N_{IG}, N_{II} , g_{IG}, and g_{II} are defined in an analogous way (note: for an isolated InAs atom on a GaAs substrate $E = 0$). The elastic energy W is given as:

$$\Delta W = W\,(\text{with atom } p) - W\,(\text{without atom } p).$$

In our simulations we use a ball and spring model with springs connecting nearest and next to nearest neighbors, with spring constants k_L and k_D respectively. W is the total elastic energy and computed by summing the energy of each spring. The computation of ΔW is rather expensive; however one can use the good approximation $\Delta W = \frac{3}{2} w_p$, where w_p is the total energy of the springs connected to atom p which is computationally faster.

The system is then evolved using rejection-free KMC.[34] After each atom hop the elastic displacement field is updated. This is accomplished using the expanding box method combined with a Fourier multigrid method.[33, 35-37]

In these calculations we take the strain of 7% from the cubic crystal substrate (GaAs) and the film (InAs), $r_0 = 2 \times 10^{13}$ s^{-1}, $E_d = 1$ eV, $g_{GG} = g_{I\,G} = 0.18$ eV, $g_{I\,I} = 0.16$ eV, $k_L = 62$ eV/a^2 , and $k_D = 30$ eV/a^2. The values for g_{GG}, $g_{I\,G}$, $g_{I\,I}$, k_L and k_D were chosen to match the bulk elastic properties of GaAs. These simulations were performed with a 128 × 128 atomic units (a.u.) matrix, and a height of 30 a.u. A half monolayer of atoms was deposited and allowed to interact with the buffer layer below, resulting in a three-dimensional morphology.

The simulations provide a model for quantum dot formation from holes. Figure 4.1 presents the simulated morphology of the film growth as a function of deposited thickness. At the smallest thickness of 0.1 ML there are small nuclei on the inner perimeter, with a few small nuclei away from the hole. At higher deposited thickness, the nuclei away from the hole disappear and the nuclei within the perimeter of the hole grow and eventually protrude. This suggests that at a critical thickness the dots in the hole absorb the dots on the flat surface.

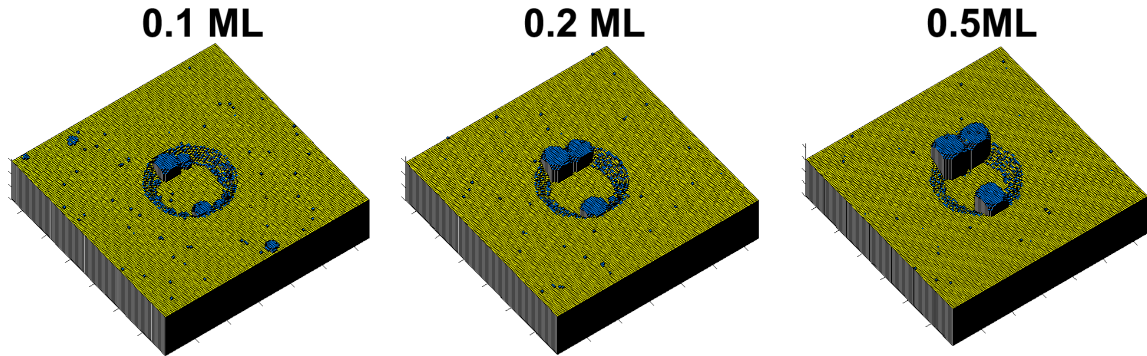

Figure 4.1: Elastic KMC simulation results as a function of deposition of InAs with the same growth parameters and starting morphology. The width of the computational cell is 128 a.u.

Next we examine different growth scenarios to understand what details about the hole geometry affect the quantum dot formation. The elastic KMC simulations were run with a minimum of four iterations at different randomizations. These four iterations were used to achieve an average number of dots nucleated per hole. The simulations show that an increase in the growth temperature from 750 K to 850 K severely suppresses the nucleation rate of quantum dots around the patterned hole of 20 a.u. in diameter, from an average of 6.0 ± 1.2 dots to 1.6 ± 0.6 dots as shown in Figure 4.2(a). This is in reasonable agreement with experimental results that will be shown later.

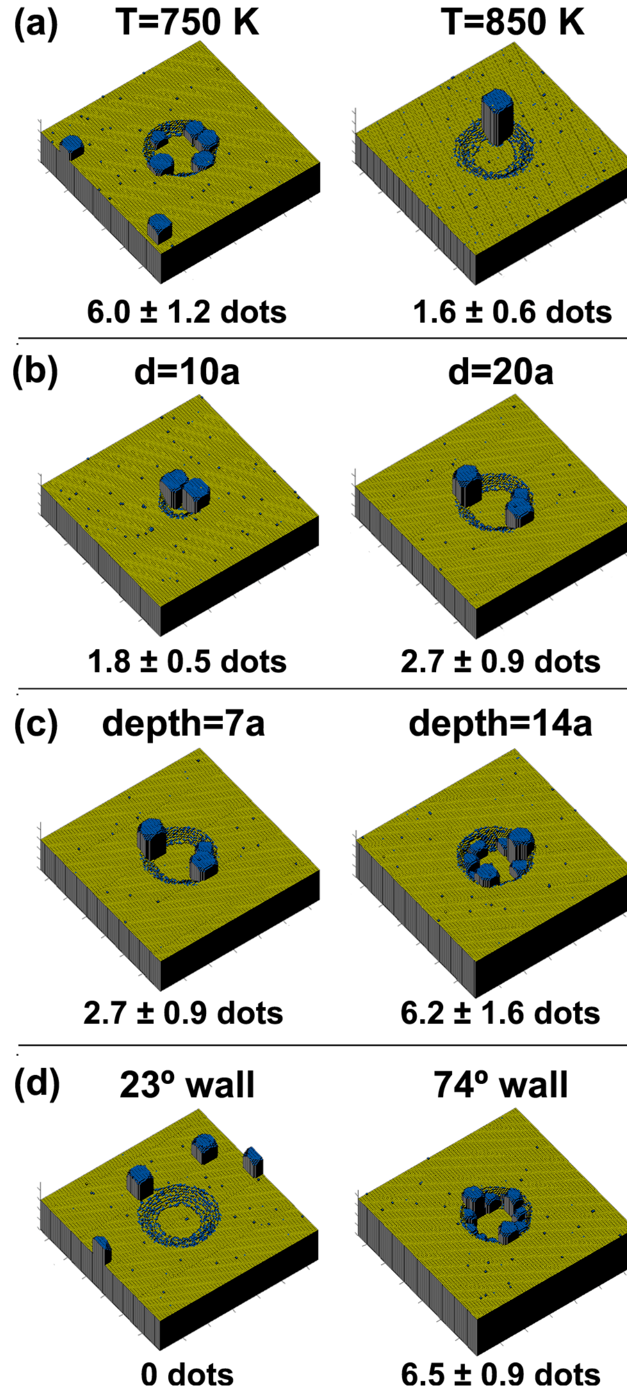

Figure 4.2: Elastic KMC simulation results for (a) varying temperature, (b) varying diameter, (c) varying depth, and (d) varying wall slope (gradual = 23°, abrupt = 74° with respect to the surface) of 0.5 ML InAs deposited on GaAs. The number of dots is for an average of at least 4 different randomizations. The width of the computational cell is 128 a.u.

Figure 4.2(b)-(d) explores the shape of the initial hole and its impact on the quantum dot growth. The diameter and depth change as a function of ion dose, but it is unclear which of these factors influence the number of quantum dots that form. Simulations give us the ability to change one parameter at a time to investigate these effects independently. When the hole diameter was doubled from 10 a.u. to 20 a.u. as shown in Figure 4.2(b), the number of quantum dots that formed increased only slightly, 2.1 ± 0.7 to 2.7 ± 0.9 dots, respectively. Figure 4.2(c) shows that doubling the depth increases the number of dots nucleating per hole from 2.7 ± 0.9 to 6.2 ± 1.6. Similarly, Figure 4.2(d) shows that when the slope of the hole wall is gradual, 27° with respect to the surface, the dots only nucleate away from the hole. But when the slope is very sharp, 74° with respect to the surface, there are many dots that form within the hole (6.5 ± 0.9). These simulations indicate that the depth and shape of the hole, and not necessarily the diameter, determines the number of quantum dots nucleated. It is useful to change a single variable at a time, but experiments do not always go so smoothly.

Experimental Details

For different starting geometries the elastic KMC simulations indicate the quantum dots nucleate within holes. We used the *in vacuo* FIB to pattern hole arrays to direct the self assembly of quantum dot on films grown on GaAs(001) substrates. Typical values for growth rates were R_{Ga}=0.30-0.75 ML/s, and R_{In}=0.10-0.25 ML/s. Two different As_4 fluxes, ~1.0 ML/s and ~2.2 ML/s, were employed to give similar V:III flux ratios while growing GaAs or InAs. All temperature measurements were made by an optical pyrometer. After oxide desorption, a 400 nm GaAs buffer layer was grown under

the higher As_4 flux at a substrate temperature of T=590 °C. The sample was then annealed at the growth temperature under a high As_4 flux and allowed to cool to room temperature under low arsenic flux. When cool, the sample was either transferred *in vacuo* to the FIB patterning system or removed from the chamber for *ex situ* FIB modification. The FIB patterned the GaAs substrate with arrays of holes with 100-560 nm spacing. Each hole was dosed in a single pass with a 30 keV, 7.5 pA beam using ion dwell times ranging from 400-2000 μs, which have predicted sputter depths on the order of a few MLs or less.[38] After irradiation, samples were returned to the growth chamber and the sample temperature was raised to T=530 °C under low As_4 flux. When the sample was FIB processed *in vacuo* it never left the vacuum system and desorption of the oxide layer is avoided. The samples prepared by *ex situ* FIB had to undergo desorption once more, and sometimes another GaAs buffer layer was grown at 590 °C. Thin layers of InAs (0.9-2.4 ML) were deposited at T=510 or 530 °C under a low arsenic flux while the surface had a c(4×4) reconstruction according to RHEED. Following growth, samples were quenched to room temperature under low As_4 flux. The surfaces of the samples were characterized *ex situ* by AFM tapping mode, using tips with a radius of curvature of 8 nm.

Results

Ex Situ FIB Processing

There are significant challenges involved with *ex situ* FIB operation because of the introduction of a surface oxide layer that was discussed previously. Once the sample

leaves the confines of the high vacuum, an oxide layer forms that needs to be subsequently desorbed. *Ex situ* FIB irradiation is advantageous because these FIBs (Nova Nanolab and Quanta 3D) have automated stage movements and can tile patterns. In order to evaluate the possibility of proceeding outside of vacuum we first needed to investigate the surface roughness associated with the desorption of the oxide layer.

Ga-assisted desorption by the MBE Ga source was performed, and the results are shown in Figure 4.3(a) and (b): a typical thermal desorption GaAs surface with root mean square roughness (rms) of 1.8 nm and a 4 ML Ga-triggered oxide desorption surface with rms 0.68 nm, respectively. Figure 4.3(b) shows a much-improved surface, but there still are pits visible.

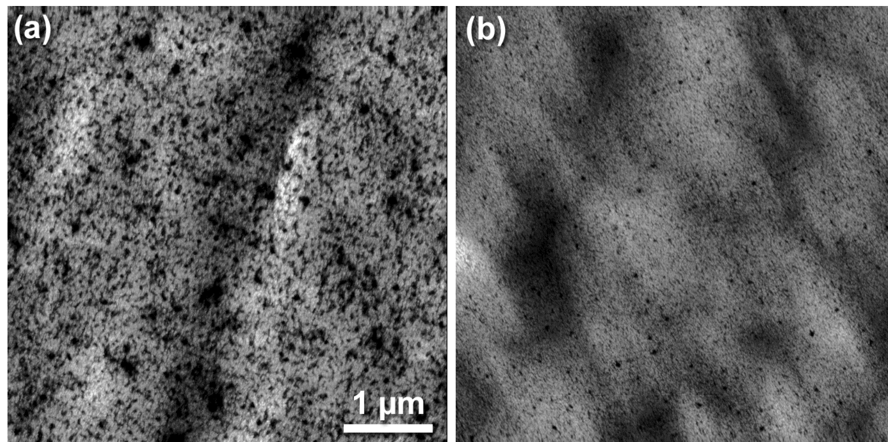

Figure 4.3: AFM images of (a) typical thermal desorption at 620 °C with rms roughness of 1.8 nm and (b) a 4 ML Ga-assisted oxide desorption with rms roughness of 0.68 nm.

Then we FIB modified a substrate with an oxide layer and then reintroduced the sample into the MBE chamber for either a combined buffer and quantum dot growth or just quantum dot growth. First we begin without any Ga-assisted desorption. We chose to deposit 1.8 ML InAs because normally FIB processing would yield quantum dots at

the FIB locations and no dots elsewhere. Figure 4.4(a) and (b) show AFM images of the resulting surfaces after thermal desorption of the oxide layer at 610 °C and 1.8 ML InAs deposited immediately after at 510 °C. It is not surprising to see a very rough surface immediately after thermal desorption. But in Figure 4.4(a) the FIB-irradiated area is noticeably smoother with rms of 1.4 nm than the surrounding area's rms of 2.2 nm. Figure 4.4(a) had FIB-induced holes with 30 nm spacing and dwell time of 28 μs. Figure 4.4(b) had a higher dwell time of 2270 μs and larger spacing of 280 nm. The FIB surface roughness (2.1 nm) did not smooth in relation to the surrounding area (1.9 nm).

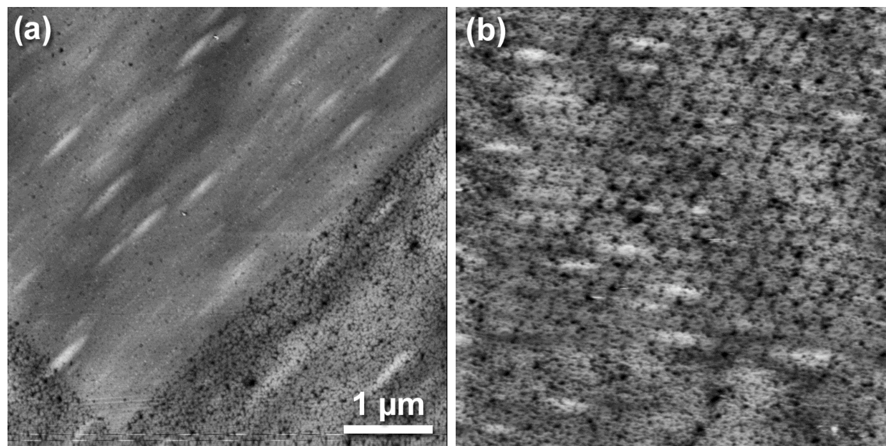

Figure 4.4: AFM images of (a) and (b) 1.8 ML InAs on *ex situ* FIB-treated GaAs that were desorbed in the MBE chamber with As overpressure. The FIB processing of (a) has hole spacings of 30 nm and dwell time of 28 μs and (b) has hole spacings of 280 nm and dwell time of 2270 μs.

During *ex situ* processing of the sample in Figure 4.4(a) there were no visible Ga droplets that formed. When ion doses are high, Ga droplets precipitate on the surface because of preferential etching of As from the local energy introduced by Ga ions from the FIB.[39] Because our FIB irradiated area has lower rms values than the surrounding area, the desorption was actually Ga assisted. During desorption, the Ga was liberated

from the FIB and assisted desorption similar to surfaces from Ga-assisted desorption.[7, 13] Asaoka has shown similar results with Ga ions helping desorb the oxide layer smoothly without any As overpressure.[6] Asaoka used blanket Ga ion irradiation to calculate the critical Ga ion dose for optimal native oxide as-received GaAs. Too high of a dose would cause milling, and too low would result in pitting of the surface from thermal desorption. The critical ion dose corresponds to a dwell time of 185 μs in our experimental setup. Figure 4.4(a) is below the critical dose and shows improvement in rms, but Figure 4.4(b) is above the critical dose and milling overtakes the Ga-assisted desorption. The FIB can be used as another vehicle for Ga ion deposition for Ga-assisted desorption. Future experiments will have to calibrate the correct Ga ion dose for the various thicknesses of oxide layers.

To improve further upon the surface roughness from the Ga-assisted oxide desorption, a GaAs buffer was deposited on top of the *ex situ* FIB-modified GaAs. Normally buffers of several hundred nanometers are grown on top of thermally desorbed surfaces, but to maintain the integrity of the FIB-induced features, the buffer should ideally be less that 100 nm thick. Buffer sizes of 10-60 nm were grown with significant surface roughening remaining, like the sample shown in Figure 4.5. This specific image has a FIB pattern of 560 nm hole spacing and 500 μs dwell time. The FIB area and surrounding area remained quite rough despite the 20 nm GaAs buffer deposited, and no InAs quantum dots could be identified in or around the area.

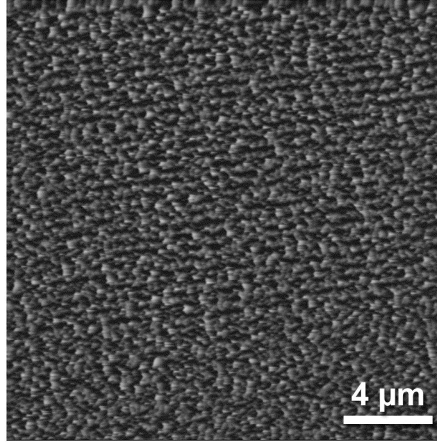

Figure 4.5: AFM image of 1.8 ML InAs on top of 20 nm GaAs buffer grown on Ga-assisted desorbed GaAs.

These *ex situ* results indicate that more care must be taken to help remove the oxide layer to leave a flatter surface. Thermal desorption is too rough for InAs quantum dots to nucleate at patterned sites. Preliminary results from Ga-assisted desorption is promising, but must be fine-tuned to achieve the smoothest surface. H-assisted desorption was not an option because the equipment is not available. A smooth surface could also be achieved by using *in vacuo* FIB to avoid the formation of an oxide layer. If the *ex situ* FIB is the only method available, then further optimization of Ga-assisted desorption of FIB patterns in combination with a small buffer layer must be performed. All of these roughness issues associated with oxide desorption can be avoided if the sample is not exposed to air between buffer growth and FIB patterning.

In Vacuo Quantum Dot Arrays

Fidelity

Because the *ex situ* FIB introduced many difficulties with surface roughness, we analyzed FIB patterns manufactured *in vacuo*. First we began with a smooth GaAs buffer layer that was transferred to the FIB, and holes were milled in the surface. Figure 4.6 shows an AFM image of a GaAs buffer layer that has been patterned with an array of holes spaced 250 nm apart and dosed with a dwell time of 800 μs per hole followed by an anneal to *T*=530 °C under low As_4 flux. The step structure of the substrate is also resolved between the holes and is apparently unperturbed by the patterning process. For this set of patterning conditions, individual holes due to ion irradiation are clearly observed that are 42 ± 13 nm in diameter and 1.7 ± 0.7 nm deep. The hole size varies, and in some instances no hole is visible at the expected location. The probability of finding a hole at the intended location, which we call the fidelity, increases as a function of ion dose (plotted in Figure 4.7) and approaches 1 for the highest dwell times (1600 μs). The fact that at lower dwell times the fidelity is not unity suggests that the hole formation process has a stochastic component. Indeed, it has been shown that the Ga ion beam initially injects point defects into the surface, which then coalesce into either a hole or an annular ring upon annealing.[40] It is possible that the beam conditions may still be optimized in order to improve the probability that exposure to the ion beam will produce the desired feature with 100% fidelity at lower dwell times.

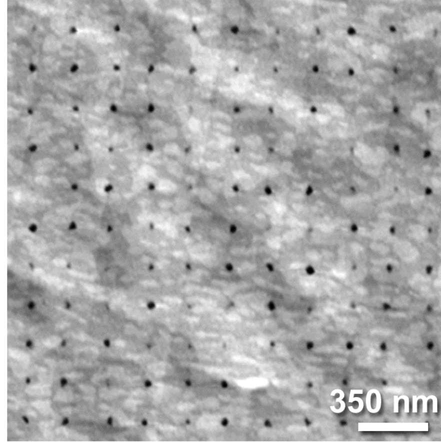

Figure 4.6: AFM image of a GaAs buffer layer that has been patterned with an array of holes spaced 250 nm apart and dosed with a dwell time of 800 μs per hole, followed by annealing at *T*=530 °C under low As_4 flux. The height scale is 3 nm.

Experimentally, the number of locations where quantum dot formation is observed is consistently less than the number of holes observed for any given dwell time (Figure 4.7). The elastic KMC simulations suggest that the holes at which no dots are observed are not necessarily annihilated during the growth of the film; rather, the quantum dots are completely within the holes and are thus undetectable by AFM. It is difficult to determine whether quantum dot growth is accurately observed experimentally because probing the interior of holes of these size scales is hard to achieve with the AFM. The AFM tips have a radius of curvature of 8 nm and can only reliably image protruding dots. Dots are only counted if they protrude from the localized surface.

In these experiments, quantum dots are not observed away from the pattern until a thickness of 2.2 ML, indicating that the pattern lowers the critical thickness for quantum dot formation.[41] It is not surprising that these FIB-induced holes act as nucleation sites in light of the fact that quantum dot formation has been observed on mesa tops[42] and at step edges[43].

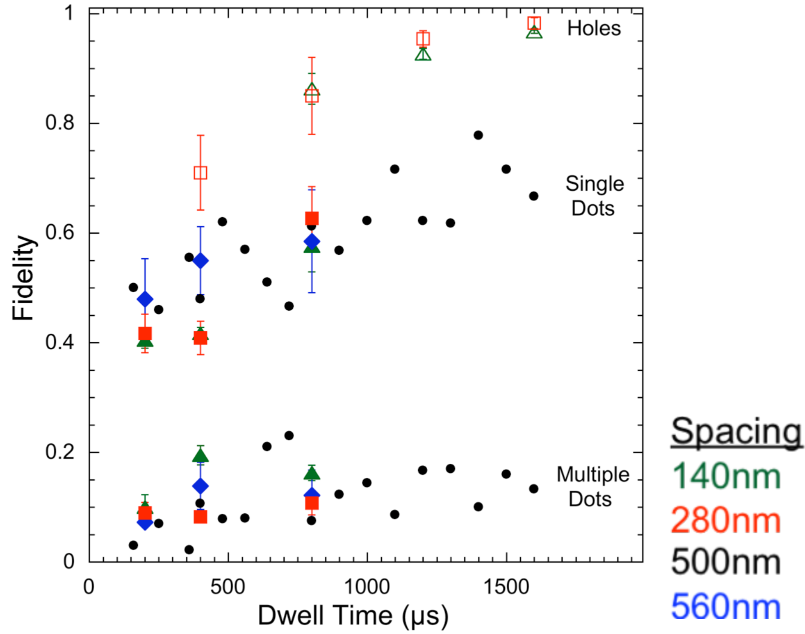

Figure 4.7: Probability of finding a hole, single quantum dot, or multiple quantum dots appearing at the intended location for a 2.0 ML-thick InAs film deposited at 530 °C for arrays with periodicity of 140 nm (green triangle), 275 nm (red square), 500 nm (black circle), and 550 nm (blue diamond).

Also tabulated in Figure 4.7 is the fidelity for different periodicities of arrays. The hole arrays have no observable effect from the array spacing on the probability of finding one or more dots at a given location for these growth conditions. Similarly, the spacing of the arrays does not have an effect on the fidelity of single dots or multiple dots.

Growth of InAs upon these patterns results in the formation of regular arrays of quantum dots with a separation dictated by the dimensions of the pattern. Figure 4.8(a) and (b) show AFM micrographs of a 2.0 ML InAs film deposited at T=530 °C upon hole arrays, patterned using various dwell times, 560 μs in Figure 4.8(a) and 1500 μs in Figure 4.8(b). In general, dots nucleate on the sites where the holes were patterned, and the probability of having a single quantum dot at the expected location increases with longer

dwell time, as shown in Figure 4.7. In some instances, the hole is still visible next to a quantum dot, which is circled in Figure 4.8(b). The probability of the formation of a single dot is lower than that of a hole for any given dwell time, but roughly follows the same slope. There is also a non-zero probability of finding more than one dot at the intended location, which increases somewhat with increasing dwell time. The number of dots increases with dwell time. A dwell time of 800 μs yields an average of 1.9 ± 0.9 dots, and a dwell time of 2000 μs yields an average of 5.8 ± 1.2 dots, which were tabulated from AFM images of one sample of 1.8 ML InAs grown at 510 ºC on a FIB-irradiated surface with holes spaced 560 nm apart. For any given dwell time, the average quantum dot diameter is somewhat larger (64 ± 29 nm at 800 μs) than the average hole diameter (42 ± 13 nm at 800 μs), and weakly increases with increasing ion dose (closed symbols in Figure 4.9).

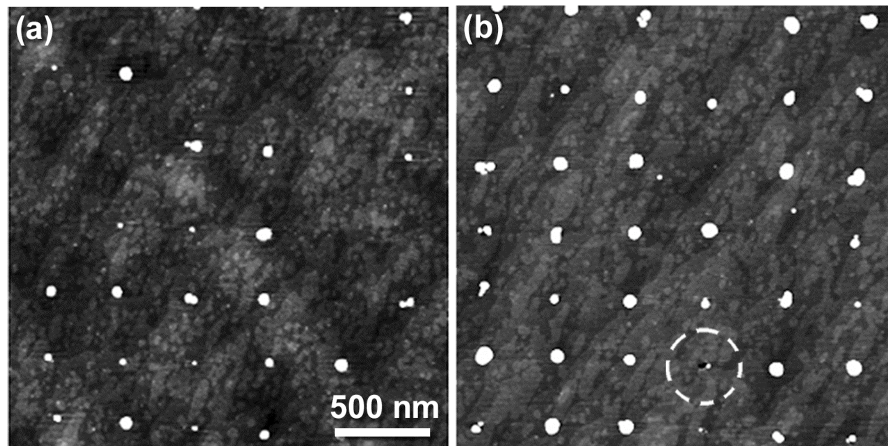

Figure 4.8: AFM images of a 2.0 ML InAs film deposited at *T*=530 °C on GaAs upon hole arrays patterned 250 nm apart and at dwell times of (a) 560 μs and (b) 1500 μs. The height scale is 10 nm. The dotted circle in (b) indicates the presence of a quantum dot next to the irradiated hole it nucleated from.

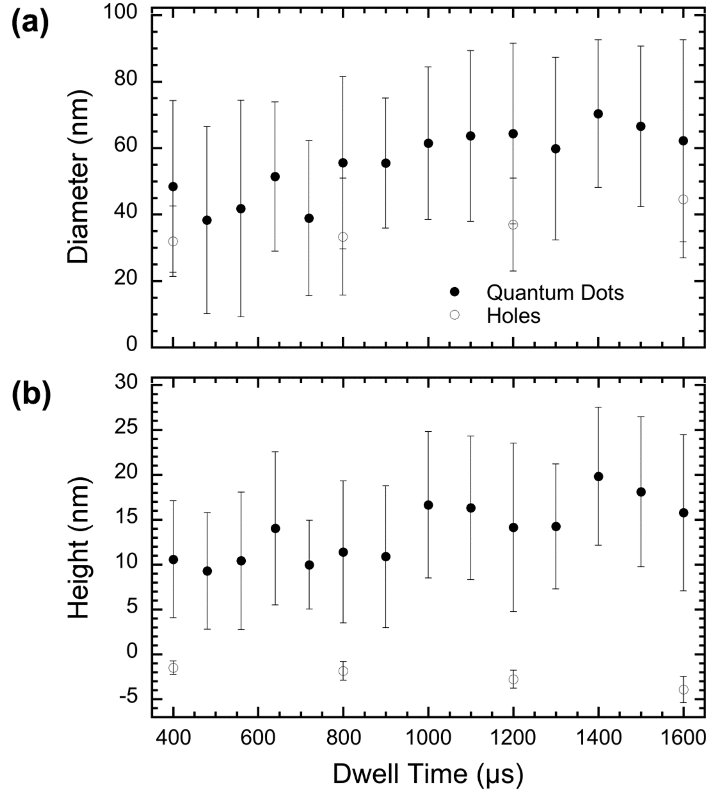

Figure 4.9: Plot of the feature (a) diameter and (b) height as a function of dwell time for holes (open circles) and quantum dots (closed circles) from 2.0 ML InAs deposited at 530 °C.

The ratio of the height to the diameter of the FIB-induced quantum dots is 0.25 regardless of the dwell time. This compares favorably to reported aspect ratios of 0.24 and absolute sizes of quantum dots self assembled without patterning.[44] This data shows that the ion irradiation or presence of any residual Ga from the ion beam has no effect on the surface energy of the system, contrary to observations of FIB-induced quantum dots in the SiGe system.[45] If the ion beam did alter the surface energy, due to deposition of excess Ga from the beam for instance, then the aspect ratio of the FIB-induced islands would be expected to be different than self-assembled islands.

Changing Growth Temperature

The number of quantum dots per hole can be manipulated by altering the growth conditions, namely lowering the growth temperature. Figure 4.10 shows a high magnification AFM image that shows the details of multiple dot nucleation. In this image, the film is 1.8 ML-thick InAs deposited upon a pattern of holes spaced 140 nm apart with a beam exposure of 1600 μs per spot and a growth temperature of 510 °C. In this lower temperature sample, many smaller dots nucleate at each hole. This is not unexpected, as the nucleation rate is higher at lower temperatures and was accurately simulated previously in Figure 4.2(a).

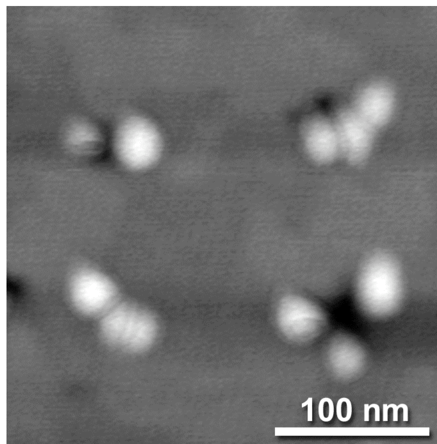

Figure 4.10: AFM image of a 1.8 ML-thick InAs film upon a pattern of holes spaced 140 nm apart and exposed to the beam 1600 μs per spot. The height scale is 15 nm.

The KMC simulations replicate experimentally observed formation of quantum dots at changing temperatures. The simulation shows that an increase in the growth temperature, 750 K to 850 K, drastically changes the number of dots nucleated around the patterned hole, from an average of 6.0 ± 1.2 dots to 1.6 ± 0.6 dots in Figure 4.2(a). This is in reasonable agreement with experimental results that show an average of 4.5 ± 1.2

dots at T=510 °C (783 K) and 1.3 ± 0.6 dots at T=530 °C (803 K) for a dwell time of 1600 μs. Quantum dots also nucleated away from the patterned hole when the temperature changed. At 750 K in the simulations, an average of 2 dots nucleated away from the patterned area and for experimentally grown samples at growth temperatures below 510 °C, AFM reveals more nucleation of quantum dots away from the holes.

Filling of Holes

The evolution of quantum dot growth can be observed when depositing larger amounts of InAs into the FIB-created holes. The elastic KMC simulations from Figure 4.1 show that the dots nucleate at the hole wall. We present similar successive growth experiments where the holes are filled by 0.9 ML and 1.5 ML InAs. AFM images are shown in Figure 4.11. The images with no InAs deposited have scanning effects that are not a part of the surface features. These samples were grown in rapid succession to limit any experimental variability. Two periodicities are presented here: 280 nm and 560 nm. The starting buffer has step height resolution and in some images large surface steps can be seen. The FIB-created holes have a fairly circular shape. Some holes are slightly elongated because of ion beam conditions. As the holes fill with 0.9 ML InAs, there is a more defined elongation of the holes. It is unclear whether this is from the initial hole shape or from preferential adhesion of the InAs. When 1.5 ML InAs is deposited, the hole turns into a star shape. The move from a circular to star shape indicates there is preferential filling within the hole walls.

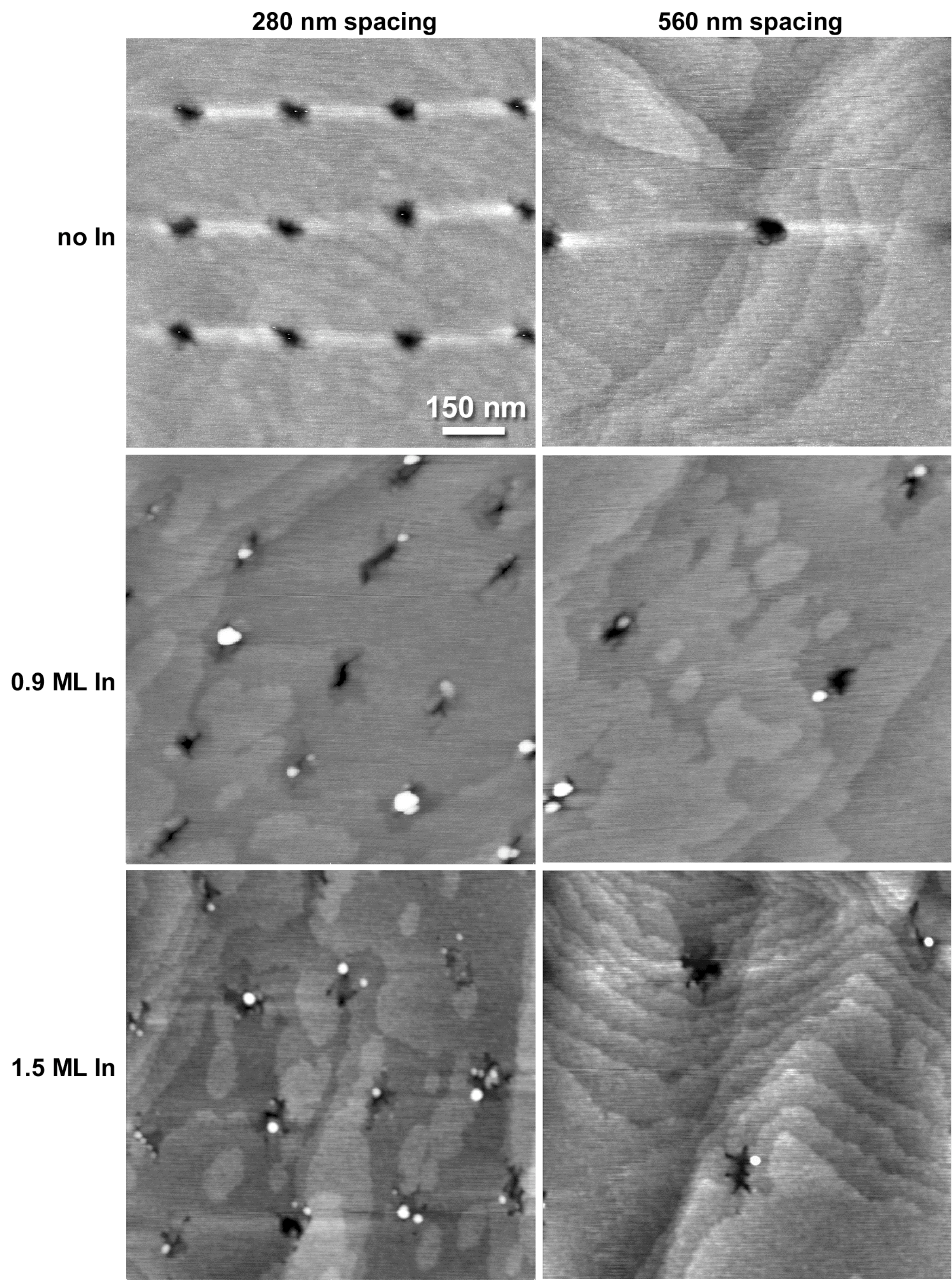

Figure 4.11: AFM images of FIB-modified arrays of GaAs at different periodicities and varying levels of InAs deposition.

Changing hole shapes has been seen with different patterns. Atkinson et al shows that buffer growth over the pattern causes the holes to morph into a figure eight along the

[110].[10] Mehta et al also see elongation of their holes occurs, but because of their very high temperature re-evaporation step, this seems more likely due to strong material transport.[29] Our elongation of holes, especially shown in the 0.9 ML InAs deposition in Figure 4.11, is most likely due to preferred deposition of InAs. At 1.5 ML InAs it is more difficult to see the elongation because more material fills the hole and obscures the shape.

From these AFM images, we can examine both the hole shapes and the quantum dot shapes. Other AFM images had varying spacings and dwell times and were analyzed but not shown. When the dwell time increased, the hole area increased, as shown in Figure 4.12, and got deeper. Figure 4.12 also indicates that the hole gets smaller when more material is deposited: 0.9 ML InAs has a smaller area than the original holes, and then 1.5 ML InAs has even smaller holes, indicating that the hole walls are filling with material.

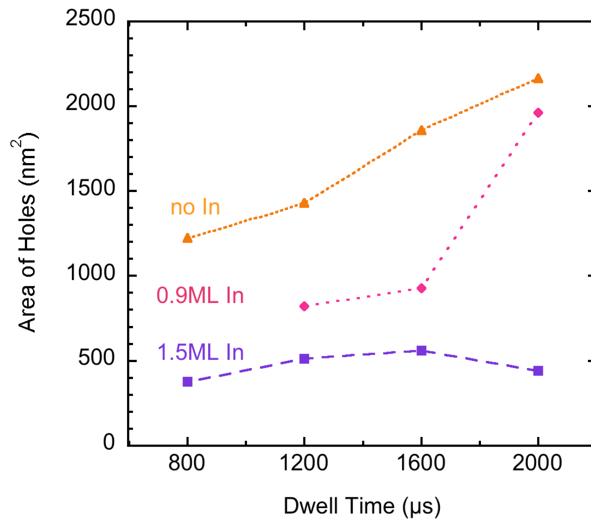

Figure 4.12: Average area of holes as a function of dwell time for the spacing of 560 nm.

At 1200 μs dwell time, the holes fill with InAs as expected and an example of a typical line profile of the hole is shown in Figure 4.13. The measured average depth of the bare hole is 3.9 ± 0.8 nm and the average depth after 0.9 ML InAs deposition is 1.4 ± 0.6nm. If all the 0.9 ML of InAs deposited within the hole fills the bottom of the hole, the new filled hole depth would be 1.5 nm, which is close to the average depth. Volumetrically for 1.5 ML InAs, the hole depth would be 1.1 nm. In Figure 4.13 the width of the hole actually widens when InAs is deposited. This is slightly different from the growth mechanism proposed by the elastic KMC simulations shown earlier in Figure 4.1. The simulations depicted growth occurring within a fixed hole, even though there is intermixing allowed. The actual deposition of the InAs may be causing surface energy relaxation and widening of the hole. Atkinson et al showed the hole profile widened with Ga-assisted desorption.[46] They did not see the hole profile change with simple annealing with As overpressure. This suggests that excess Ga on the surface preferentially migrates to the hole to fill the As-terminated steps. At higher temps the widening and shallowing of holes is even more pronounced due to the increased mobility of the Ga. The Ga that is not consumed by the surface oxide migrates to the bottom of the hole, where the concave shape has a lower surface energy. In our experiments, there is a similar effect where intermixing from the hole walls during In deposition allows the Ga to reduce its strain energy by moving to the hole bottoms.

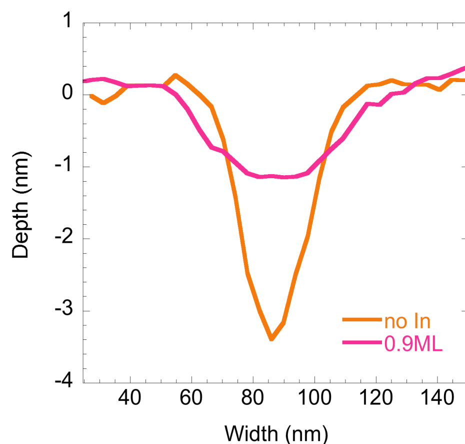

Figure 4.13: Average line profile of a hole filled by 0.9 ML InAs for 1200 μs dwell time and 560 nm spacing.

Hole and Quantum Dot Size

Holes can be characterized by their surface width and depth, and at lower doses, fidelity as previously shown in Figure 4.7. The width and depth according to ion dwell time are shown in Figure 4.9(a) and (b) as open circles. Increasing ion dose causes larger hole sizes and deeper penetration. The open symbols in Figure 4.9a show that the diameter of the holes increases from 30 ± 10 to 40 ± 18 nm as the dwell time changes from 400 to 1600 μs. The depth increases from 1.5 ± 1 to 4 ± 2nm over the same range in ion dose (open symbols in Figure 4.9b). However, it should be noted that when the holes become very narrow and deep, AFM is limited in its ability to accurately measure their true depth.

Obtaining reliable quantum dot sizes is important in achieving device efficiency; more uniform dots create a narrower PL emission. We examine the quantum dot sizes in Figure 4.9(a) and (b), where the width and height are designated as filled circles of 2.0 ML InAs quantum dots. Figure 4.9 clearly shows that the diameter and depth increase with increasing ion dose, but it is not entirely clear which affects the formation of the

quantum dots. The elastic KMC simulations allowed us to alter one parameter to see how that quantum dot growth changed. The hole diameter was doubled in with a mild increase of the number of dots. The depth and slope of the hole wall are much more critical factors in the number of dots formed. The elastic KMC simulations show that the driving force of the increasing number of quantum dots per feature seems to be largely attributed to the depth and slope of the initial hole.

Changing Periodicity

Another growth parameter we could change is the periodicity. We showed that the periodicity of the hole array does not affect the probability of finding a dot at the intended location for 2.0 ML InAs in Figure 4.7. Unfortunately the elastic KMC simulations cannot be enlarged to accommodate changing periodicity without moving to an elastic continuum model. Without simulations, to investigate the formation of growth, we can instead look at lower amounts of InAs deposited as a function of periodicity. Thus we further examine the mechanism of the InAs nucleation on the holes in Figure 4.11. When larger amounts of InAs are deposited on the sample, the holes fill and the area is reduced. At 1.5 ML InAs deposition, the filling of the holes is most apparent, where the holes become less circular and look much more irregular. Hole sizes increase with dwell time and fill accordingly with deposited InAs, as shown in Figure 4.12. There is also a correlation between periodicity and hole size that is tabulated in Figure 4.14. There are very large standard deviations because of the large distribution of quantum dots of many different sizes. At low periodicities the width of holes appears to be smaller. When hole widths have average diameters of 50 nm, achieving smaller spacings becomes

difficult, as there is an ion beam tail that begins to overlap, creating a doubly dosed zone of ion irradiation. Also, as shown in the AFM images in Figure 4.15, the beam blanking conditions were not ideal and instead of making discrete holes at smaller spacings of 100 nm, the beam created incidental trenches. When the holes are visible in the 0.9 ML InAs sample, they appear to shrink proportionally to the original hole size. The 1.5 ML InAs sample has an almost constant depth for its holes regardless of the spacing of the holes, but they do get wider. At 0.9 ML, there is sometimes quantum dot formation, leaving some holes very large. But at 1.5 ML there is a much higher fidelity and every site has multiple dots. Overall the shape of the holes changes to a wider and shallower hole as depicted in Figure 4.13, if it does not get filled with quantum dots.

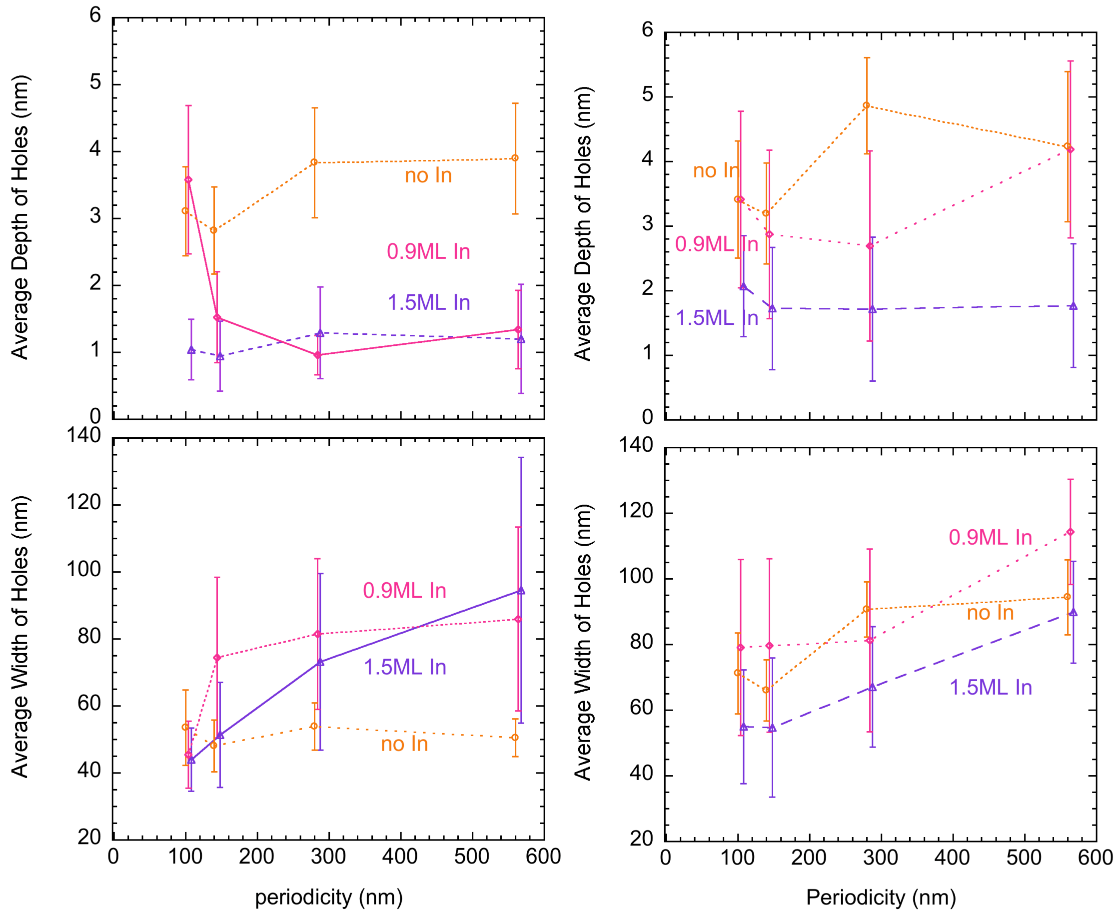

Figure 4.14: Depths and widths for holes, 0.9 ML InAs, and 1.5 ML InAs. Left: dwell time=1200 μs; right: dwell time=2000 μs

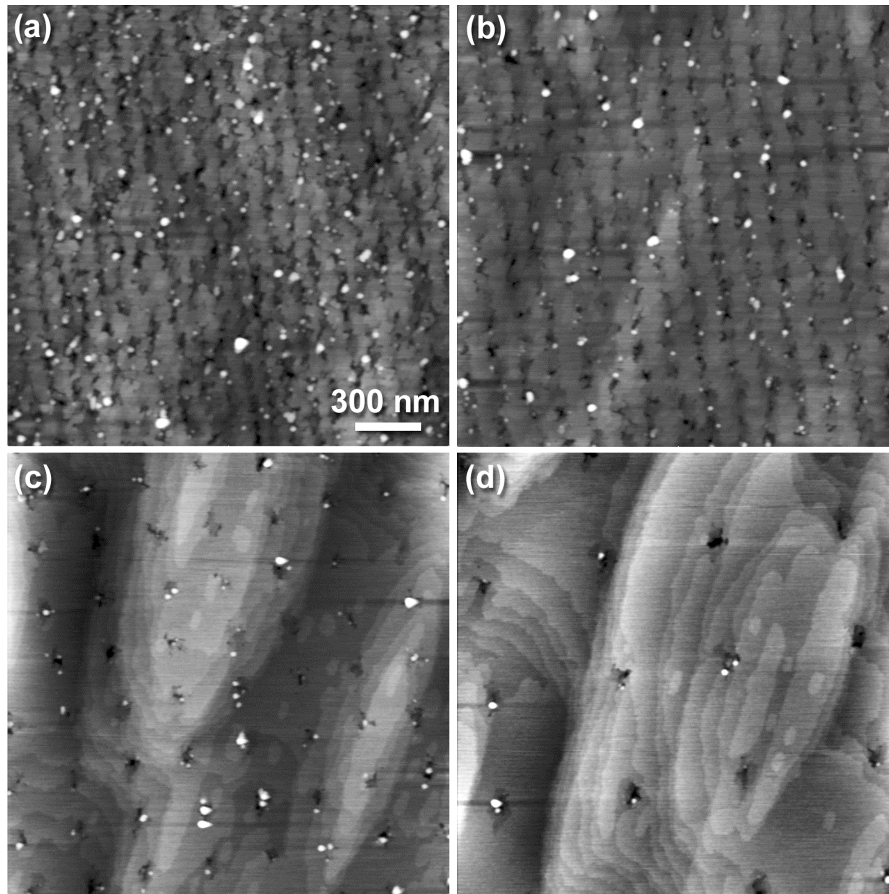

Figure 4.15: AFM images of 1.5 ML InAs on GaAs with a FIB dwell time of 2000 µs at different hole spacings (a) 100, (b) 140, (c) 280, and (d) 560 nm.

The quantum dots that form are of many different sizes and fidelity. When 0.9 ML is deposited the quantum dots formed are higher and wider than the dots formed when 1.5 ML is deposited. Figure 4.16 shows the average dot height and width for the 0.9 ML and 1.5 ML of InAs grown on the FIB samples for different periodicity. The lower deposited material 0.9 ML has larger dots, although there are fewer dots. The 0.9 ML has an average of 0.7 ± 0.7 dots per hole and 1.5 ML has an average of 1.7 ± 0.9 dots per hole. The 1.5 ML results in smaller dots but more of them. This is not in agreement with the growth mechanisms shown in Figure 4.1. These results suggest that the larger

dots at 0.9 ML somehow spread out and become smaller. Growth kinetics would normally indicate that small dots would coalesce as more material is deposited. This must be looked at more closely in future experiments. Perhaps the star-shaped filling of the holes created more nucleation sites for the quantum dots to form. But because the error bars are so large, it is difficult to assume any of these trends to be true.

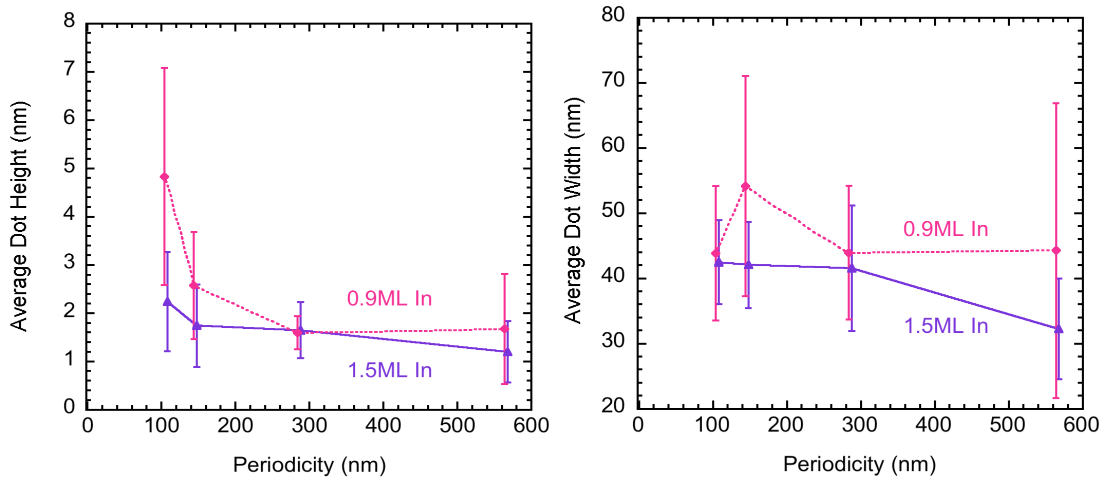

Figure 4.16: Average quantum dot height and width varied by periodicity at a constant dwell time of 1200 μs.

Conclusions

The first step in obtaining reproducible uniform InAs quantum dots is to characterize what varying growth conditions and starting patterns produce. We can then begin to understand the mechanisms behind the quantum dot growth in order to place them where we want and what size dots we want.

We showed *ex situ* FIB patterning is not a viable option for our samples because more calibration needs to be performed to perfect the Ga-assisted desorption and buffer overgrowth. An elastic KMC model was used to simulate growth of location, size, and

number of dots by changing growth conditions and hole geometry. This model worked well to explain the multiple quantum dots that formed with various hole shapes. In vacuo FIB patterning was used to vary growth temperature, dwell time, periodicity, and deposition amount. Size, fidelity, and quantity of dots depended greatly on the dwell time. If the ion dose is too low, holes may not appear. Increased ion doses deepened holes and increased fidelity. Multiple quantum dots form at a hole site when the temperature is lowered. We then looked at hole and dot shapes when increasing amounts of InAs are deposited to better understand the growth mechanisms involved in quantum dot formation. When InAs was grown, holes filled accordingly with depth, but they also widened, indicating that surface energy is relaxing. The effect of periodicity on quantum dot growth is still not yet fully understood.

These results are a starting point and have shown that our quantum dots still have a large range of sizes and have unexpected heights and diameters. Future experiments could focus on reliable reproduction of specific quantum dot sizes.

References

[1] Levi A C and Kotrla M. 1997 *J Phys-Condens Mat* **9** 299-344

[2] Kratzer P, Penev E and Scheffler M. 2003 *Appl Surf Sci* **216** 436-446

[3] Joyce B A, Vvedensky D D, Bell G R, Belk J G, Itoh M and Jones T S. 1999 *Mat Sci Eng B-Solid* **67** 7-16

[4] Caflisch R E, Weinan E, Gyure M F, Merriman B and Ratsch C. 1999 *Phys Rev E* **59** 6879-6887

[5] Elsholz F, Meixner M and Scholl E. 2003 *Nucl Instrum Meth B* **202** 249-254

[6] Asaoka Y. 2003 *J Cryst Growth* **251** 40-45

[7] Wasilewski Z R, Baribeau J M, Beaulieu M, Wu X and Sproule G I. 2004 *J Vac Sci Technol B* **22** 1534-1538

[8] Ballestad A, Ruck B J, Schmid J H, Adamcyk M, Nodwell E, Nicoll C and Tiedje T. 2002 *Phys Rev B* **65** ARTN 205302

[9] Petit E J and Houzay F. 1994 *J Vac Sci Technol B* **12** 547-550

[10] Atkinson P, Kiravittaya S, Benyoucef M, Rastelli A and Schmidt O G. 2008 *Appl Phys Lett* **93** ARTN 101908

[11] Proix F, Sebenne C A, Cherchour M, Mhamedi O and Lacharme J P. 1988 *J Appl Phys* **64** 898-902

[12] Cheng C C, Meneou K and Cheng K Y. 2009 *Appl Phys Lett* **95** ARTN 173108

[13] Lee J H, Wang Z M and Salamo G J. 2006 *J Appl Phys* **100** ARTN 114330

[14] Taylor C, Marega E, Stach E A, Salamo G, Hussey L, Munoz M and Malshe A. 2008 *Nanotech* **19** ARTN 015301

[15] Kapsa J, Robach Y, Hollinger G, Gendry M, Gierak J and Mailly D. 2004 *Appl Surf Sci* **226** 31-35

[16] Song H Z, Usuki T, Hirose S, Takemoto K, Nakata Y, Yokoyama N and Sakuma Y. 2005 *Appl Phys Lett* **86** ARTN 113118

[17] Garcia R, Martinez R V and Martinez J. 2006 *Chem Soc Rev* **35** 29-38

[18] Lee S C, Stintz A and Brueck S R J. 2002 *J Appl Phys* **91** 3282-3288

[19] Hahn C K, Park Y J, Kim E K, Min S-K, Jung S K and Park J H. 1998 *Appl Phys Lett* **73** 2479-2481

[20] Schneider C, Huggenberger A, Sunner T, Heindel T, Strauss M, Gopfert S, Weinmann P, Reitzenstein S, Worschech L, Kamp M, Hofling S and Forchel A. 2009 *Nanotech* **20** ARTN 434012

[21] Lugstein A, Basnar B and Bertagnolli E. 2004 *Superlattices Microstruct* **36** 107-111

[22] Kim S-W, Kotani T, Ueda M, Fujita S and Fujita S. 2004 *Physica E* **21** 601-605

[23] Lopez R, Suh J Y, Feldman L C and Haglund R F. 2004 *Mater Res Soc Symp P* **820** 319-324

[24] Du Y G, Groves J F, Lyubinetsky I and Baer D R. 2006 *J Appl Phys* **100** 094315

[25] Gray J L, Hull R and Floro J A. 2006 *J Appl Phys* **100** 84312-84311

[26] Karmous A, Cuenat A, Ronda A, Berbezier I, Atha S and Hull R. 2007 *Appl Phys Lett* **85** 6401-6403

[27] Yokota H, Tsunashima K, Iizuka K and Okamoto H. 2008 *J Vac Sci Technol B* **26** 1097-1099

[28] Ishikawa T, Kohmoto S, Nishikawa S, Nishimura T and Asakawa K. 2000 *J Vac Sci Technol B* **18** 2635-2639

[29] Mehta M, Reuter D, Melnikov A, Wieck A D and Remhof A. 2007 *Appl Phys Lett* **91** 123108

[30] Orr B G, Kessler D A, Snyder C W and Sander L. 1992 *Europhys Lett* **19** 33

[31] Lam C H, Lee C K and Sander L M. 2002 *Phys Rev Lett* **89** 16102

[32] Lung M T, Lam C H and M. S L. 2005 *Phys Rev Lett* **95** 086102

[33] Baskaran A, Devita J P and Smereka P. Kinetic Monte Carlo Simulation of Strained Heteroepitaxial Growth with Intermixing. submitted. In press 2009.

[34] Blue J L, Beichl I and Sullivan F. 1995 *Phys Rev E* **51** R867-R868

[35] Russo G and Smereka P. 2006 *J Comp Phys* **214** 809

[36] Russo G and Smereka P. 2006 *Multiscale Model Sim* **5** 130-148

[37] Schulze T P and Smereka P. 2009 *J Mech Phys Solids* **57** 521-538

[38] Menzel R, Bachmann T and Wesch W. 1999 *Nucl Instrum Meth B* **148** 450-453

[39] Lipp S, Frey L, Lehrer C, Frank B, Demm E and Ryssel H. 1996 *J Vac Sci Technol B* **14** 3996-3999

[40] Portavoce A, Kammler M, Hull R, Reuter M C and Ross F M. 2006 *Nanotech* **17** 4451-4455

[41] McKay H, Rudzinski P, Dehne A and Millunchick J M. 2007 *Nanotech* **18** 455303

[42] Heitz R, Ramachandran T R, Kalburge A, Xie Q, Mukhametzhanov I, Chen P and Madhukar A. 1997 *Phys Rev Lett* **78** 4071-4074

[43] Placidi E, Arciprete F, Sessi V, Fanfoni M, Patella F and Balzarotti A. 2005 *Appl Phys Lett* **86** ARTN 241913

[44] Yamaguchi K, Kaizu T, Yujobo K and Saito Y. 2002 *J Cryst Growth* **237-239** 1301-1306

[45] Portavoce A, Hull R, Reuter M C and Ross F M. 2007 *Phys Rev B* **76** 235301

[46] Atkinson P and Schmidt O G. 2009 *J Cryst Growth* **311** 1815-1818

CHAPTER 5 – Optoelectronic Properties of FIB-Induced InAs Quantum Dots

In the last chapter we characterized the InAs quantum dots produced by FIB. We looked for a predictable size outcome for different growth and ion beam conditions. This material system is of particular interest because of its small bandgap of 0.417 eV, as shown in Table 5.1. Because of InAs's small bandgap it is an ideal candidate for telecommunication applications, which are in the short-wavelength infrared range of 1400-3000 nm.[1] Alloys of $In_xGa_{1-x}As$ can be tuned to various bandgap energies from 0.417-1.519 eV.

Material	Bandgap (eV)	PL Wavelength (nm)
AlAs	3.099	400
GaAs	1.519	816
InP	1.424	871
GaSb	0.812	1527
InAs	0.417	2974

Table 5.1: Bandgap energies and corresponding PL wavelength emission for relevant III-V semiconductors at 0 K.[2]

Currently most lasers, such as those used in laser pointers and compact disc players, are laser diodes. These use quantum wells, but quantum wires and dots can

improve the efficiency of the materials. Efficiency is further improved when quantum dot sizes are uniform and the range of the bandgap becomes much smaller. The capability to place quantum dots precisely also enhances device efficiency.

In this chapter we investigate the potential for these FIB-induced InAs quantum dots for optoelectronic devices. We evaluate the PL emission of the quantum dots by using micro PL and spatial mapping. These PL testing setups have been described in Chapter 2. Then we look at the crystal structure in the TEM to examine the defects from the ion beam.

Background

PL of Assembled Dots

There have been many methods to induce assembly of quantum dots and obtain successful PL emission. Regular self assembled InAs quantum dots have been studied intensively to optimize the growth conditions to yield excellent PL results: 1265 nm (0.98 eV) at 300 K[3], 1024 nm (1.21 eV) at 2 K[4] and 7 K[5], and at 950 nm (1.3 eV) for 80 K[6]. Groups have also grown InAs on cleaved surfaces to produce 940 nm (1.32 eV) at 10 K.[7] InAs quantum dots have also been placed in InGaAs quantum wells to yield strong PL emission at 1240-1305 nm (0.95-1.0 eV).[8, 9] Stacked quantum dots have shown dramatic changes in the PL emission.[3, 10]

There has also been extensive research on the manipulation of the surface to directly assemble InAs quantum dots on GaAs. *In situ* modification by electron beams has been performed: *in vacuo* traditional electron beam lithography gave PL emission at 1130 nm (1.1 eV) at 5 K[11] and a very long electron beam irradiation by RHEED

improved PL at 1000 nm (1.24 eV) at 50 K[12]. The majority of experiments performed patterning *ex situ*. A variety of methods of surface patterning was used to create PL emission of InAs quantum dots at 1305 nm (0.95 eV) at 300 K by nanoimprint lithography[13], 1300 nm (0.95 eV) at 10 K by AFM probe oxidation and subsequent etching[14], and 1050 nm (1.18 eV) at 77 K by electrochemical etching[15]. Electron beam lithographic surfaces have been spatially mapped to show strong InAs quantum dot emission from the etched surface at 940 nm (1.32 eV) at 8 K[16] and 1030 nm (1.20 eV)[17].

There are some studies of FIB irradiated surfaces and the resulting PL emissions.[18-20] Bellini et al used the FIB after the InGaAs/GaAs structure was grown to remove a Ti mask, thus inducing damage below into the GaAs cap.[19] The PL showed suppression of the previously seen 1160 nm wavelength (1.07 eV) at 10 K. A more similar study shows that *in vacuo* FIB irradiation of the GaAs buffer yielded InAs quantum dots with PL spectra.[20] Mehta et al implanted both Ga^+ and In^+ ions into arrays to show that increasing ion dose yields stronger PL emission of quantum dots at 1050 nm (1.18 eV) at 77 K at an excitation power of 3 mW.

TEM to Investigate Defects

The implantation of ions has been used for several decades now and is prevalent in all silicon- and GaAs-based devices. Small doses of implantation are used as dopants and larger doses cause intentional compositional disordering.[21] High amounts of ion irradiation cause many defects within the crystal lattice. Dislocation loops via TEM images have been shown in many materials: in the GaAs system, ions of Kr or Be[22],

ions of Al or Si[23], ions of Ar[24, 25], ions of Be, Mg, Si, or Se[26]; and in Si, ions of Ga[27]. Besides dislocations, twinning defects and stacking faults are also shown in TEM images within the GaAs system.[25, 28-30]

If defects are present, the performance of the material is severely compromised.[18, 19, 31, 32] Cross-sectional TEM images allow us to understand how the crystal structure affects the photoluminescent properties of the samples we create and the viability of these methods for future applications.

We have alluded to the damage that FIB can inflect on its patterns. Ion implantation is the main drawback to FIB processing. TEM images of GaN pyramids grown by Gierak et al on top of 1 μm FIB holes in a Si_3N_4 mask on AlN had many threading dislocations.[33] We will address FIB's damaging effects in this chapter.

Photoluminescence Results

Samples for micro PL were also grown to examine the optical activity of the FIB-directed quantum dots. These samples were grown similar to those described before, except a 10-period 2.5 nm-GaAs/2.5 nm-AlAs superlattice was deposited prior to the quantum dot layer in order to isolate and amplify the PL emission from the InAs only.[3] After substrate desorption, a 400 nm GaAs buffer layer is grown. One of the 10-period GaAs/AlAs superlattices is grown. After the superlattice, a 30 nm GaAs buffer is grown and then FIB modified. The samples were then placed back into the chamber, and 1.8 ML InAs was deposited at T=510 °C and capped with 8 nm GaAs. Then the growth temperature was raised to 590 °C to grow another 22 nm of GaAs, followed by the same

10-period GaAs/AlAs superlattice, and 10 nm GaAs on the very top. A cross-sectional schematic of the sample is provided in Figure 5.1.

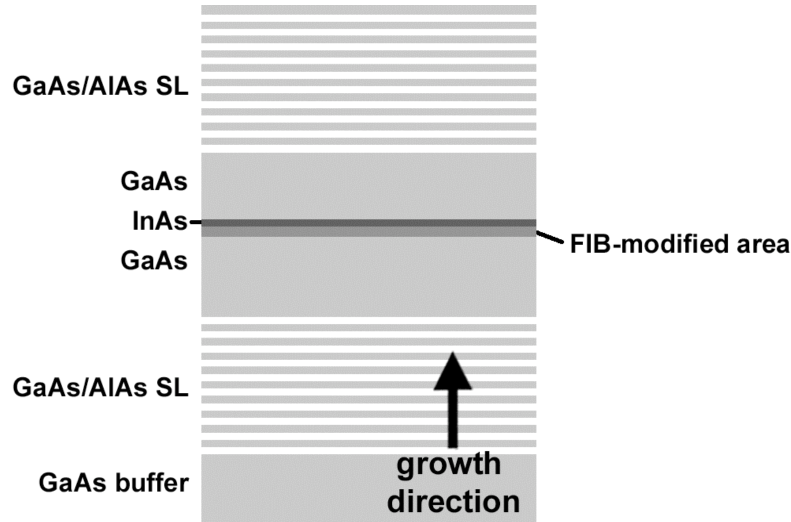

Figure 5.1: Cross-sectional schematic of PL samples grown with GaAs/AlAs superlattices.

The uncapped version of the PL samples is shown in Figure 5.2. Only 1.8 ML of InAs was deposited on top of GaAs buffers. The surfaces were FIB treated with 30 nm spacing and dwell times ranging from 15-30 μs, which is significantly different than the hole arrays presented in Chapter 4. The spacing of the FIB at 30 nm creates more of a uniform blanket irradiation, in contrast to the 100-560 nm discrete arrays. The dwell times are much lower (15-30 μs vs. 200-2000 μs) because the ion beam overlaps itself. At these ion beam conditions, the InAs quantum dots still only appear on the FIB-irradiated areas. There is a large distribution of dots of various sizes in all three AFM images in Figure 5.2. Diameters are 30 ± 10 nm, and heights are 2 ± 1 nm. The dot density at the highest dose of 30 μs in Figure 5.2(a) is 4.5×10^9 dots/cm^2 and decreases to approximately half 2.0×10^9 dots/cm^2 at 15 μs. In these experiments, quantum dots are

also not observed away from the pattern until a thickness of 2.2 ML, indicating that the pattern lowers the critical thickness for quantum dot formation.[34]

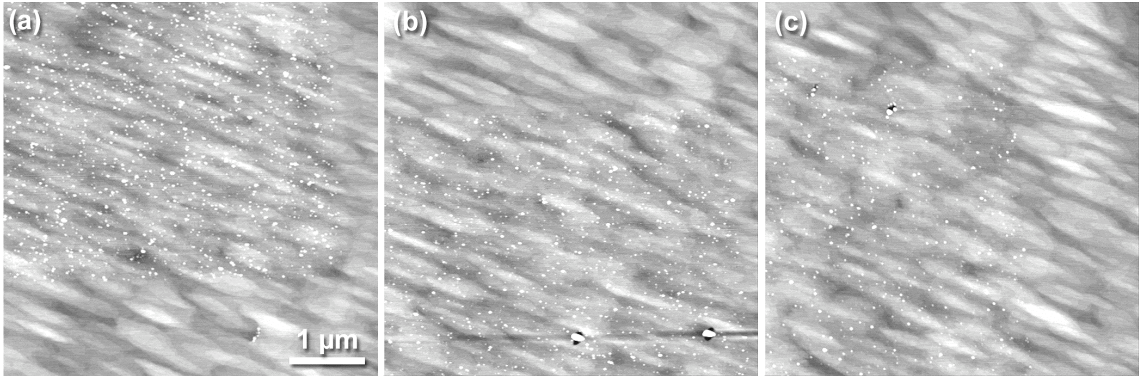

Figure 5.2: AFM images of uncapped 1.8 ML InAs on FIB modified surfaces of 30 nm spacing and dwell times of (a) 30, (b) 20, and (c) 15 µs.

Two sets of PL measurements were taken of this sample, and details can be found in Chapter 2. The Ku PL setup had a 532 nm continuous wave laser with 15 mW power at the sample, which was liquid nitrogen cooled to 77 K. Single scans of 800-1200 nm wavelengths were measured at various locations on the sample. Figure 5.3(a) shows the various locations measured on the sample and their resulting PL spectra with intensity in arbitrary units (a.u.) in Figure 5.3(b). All PL spectra have a GaAs peak at 850 nm (1.49 eV). Away from the edge of the sample, spectra show an In wetting layer present and the FIB modifications at locations A and B suppress the PL of the In wetting layer. Near the edge of the sample, no In wetting layer exists, but instead an a very wide InAs quantum dot peak is at 1030 nm (1.20 eV) with a full width at half maximum (FWHM) value of 90 nm (0.11 eV). It is unclear whether the FIB suppressed or enhanced the peak. Further PL with the Sih setup will explain what is happening near the edge of the sample.

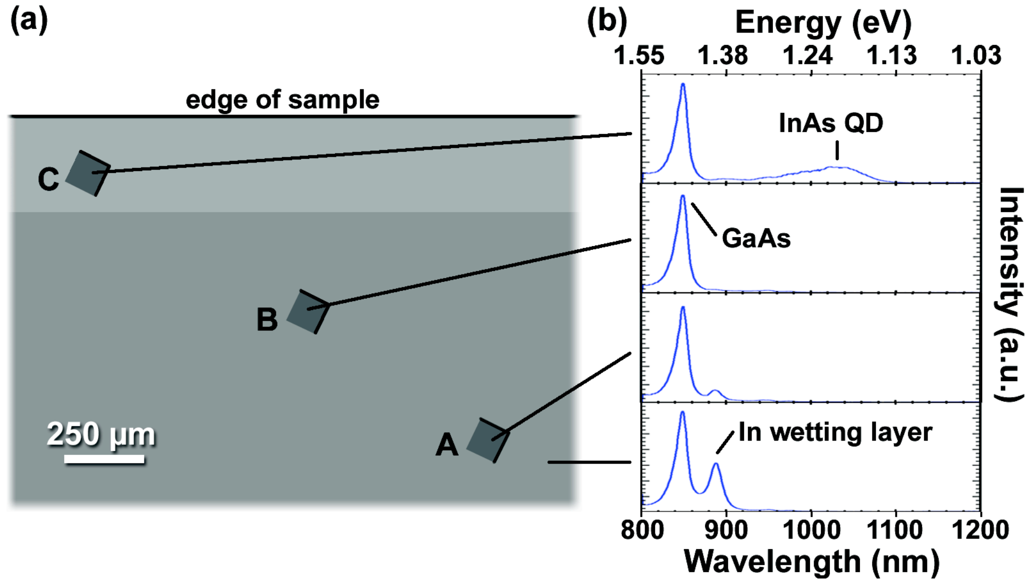

Figure 5.3: Using the Ku PL setup (532 nm wavelength with 15 mW power at 77 K), (a) an overview of the sample surface where FIB irradiation occurred and (b) the resulting PL within those areas. C, B, and A in (a) refer to FIB irradiated areas with 30 nm spacing with a 30 kV, 7.5 pA ion beam and dwell times of 10, 20, and 30 µs respectively.

In the Sih PL setup, the mode-locked Ti:Sapphire laser was tuned to 730 nm wavelength with 0.4 mW power at the sample. The sample was liquid helium cooled to 10 K. Figure 5.4(a) shows the locations of interest and their PL spectra in Figure 5.4(b). Because the sample was cooled more than the Ku setup, the GaAs peak is now at 830 nm (1.49 eV) because there is more energy needed for emission. Similarly, the PL spectra show the presence of an In wetting layer away from the sample edge. This is also suppressed by the FIB in locations A and B. The InAs quantum dot peak is visible at many different locations near the sample edge, and the In wetting layer is missing. The InAs quantum dot peak is at 980 nm (1.27 eV) with FWHM of 70 nm (0.09 eV). In the Sih setup, the InAs peak is not visible at all in the FIB-irradiated location C. Perhaps if

the excitation power were higher, there would still be a peak visible as the Ku setup showed.

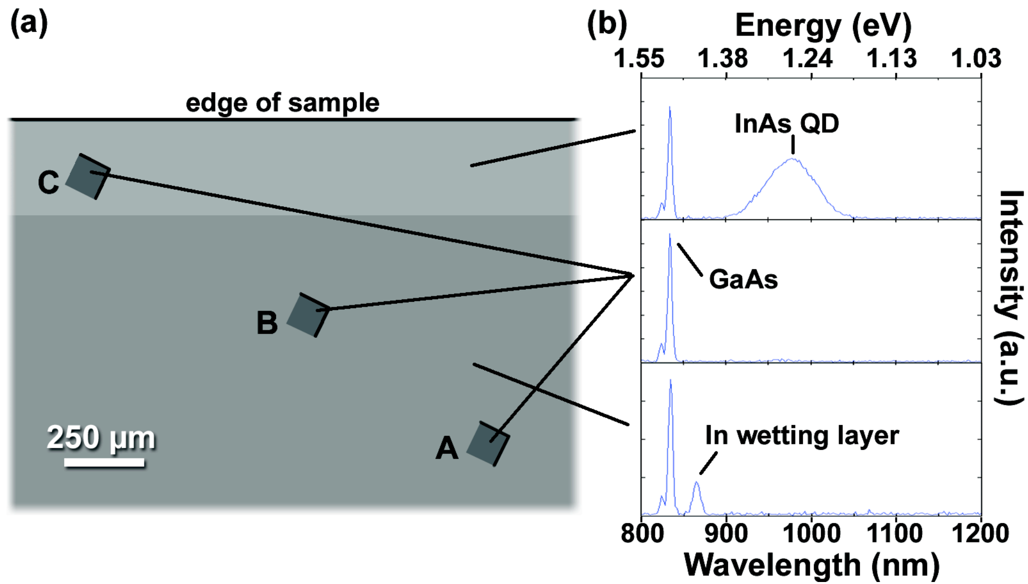

Figure 5.4: Using the Sih PL setup (730 nm wavelength with 0.4 mW power at 10 K), (a) Overview of the sample surface where FIB irradiation occurred and (b) the resulting PL within those areas. C, B, and A in (a) refer to FIB irradiated areas with 30 nm spacing with a 30 kV, 7.5 pA ion beam and dwell times of 10, 20, and 30 µs respectively.

The edge of the sample has a strong InAs quantum dot PL emission. Surface edges act as sinks for steps and can create spatially ordered PL-emitting InAs quantum dots at the very edge of GaAs.[11, 35] The width of the peak is likely due to the wide size distribution observed in these samples, which we hope to control by optimizing the patterning process. These results are similar to those found for quantum dots assembled without patterning. For example, regular self-assembled InAs quantum dots had PL emission at 950-1025 nm (1.21-1.3 eV) from 2-80 K[4-6].

To understand the PL near the edge of the sample, with the Sih setup the fast steering mirror was used to take spatial scans. Every 7 µm step a single PL spectrum was

produced across 49 μm x 49 μm areas. In this way a map was created as a function of the InAs quantum dot peak produced at 980 nm, which was the only peak visible other than the GaAs cladding peak. Figure 5.5 shows two different spatial maps created by the fast steering mirror. The peak at 980 nm was normalized to the GaAs peak at 830 nm. These results indicate that the FIB irradiation introduced defects so that the PL emission was quenched. The area where the FIB uniformly irradiated the surface shows no instance of an InAs peak, even at this lower excitation powered setup. At higher excitations, there may be an InAs peak[7] shown like in Figure 5.3, but these maps show that in these instances the FIB definitively does hinder the PL emission.

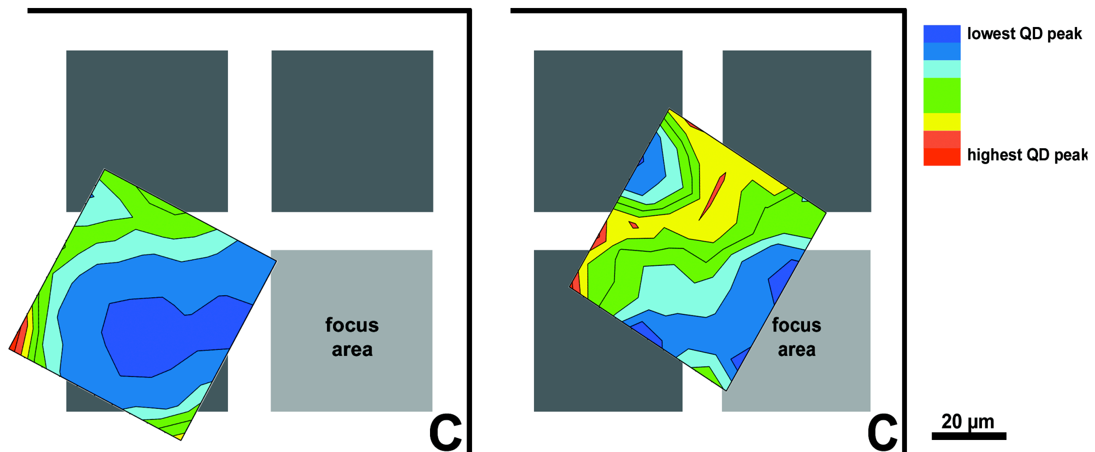

Figure 5.5: Two different PL spatial maps of the InAs quantum dot peak taken at various positions across the FIB-irradiated areas using a fast steering mirror.

In the case of Mehta et al the ion beam conditions were slightly different.[20] Their study focused on arrays while these samples were of uniform irradiations. In our work, other PL samples of dot arrays were measured with no InAs peak visible. Mehta et al also used high doses: 690,000 ions/spot correspond to 20,000 μs/spot for our beam conditions (12 nm diameter, 5.4 pA, 30 kV). The critical difference between our data and Mehta's is the introduction of a re-evaporation step. Mehta et al grew 3-5 nm of GaAs at

760 °C. This step was introduced to remove FIB-induced defects from the crystal lattice. In the next part we will show that this may have been a critical omission. The FIB may have contributed many factors to the failure of InAs PL emission. There could be implantation, interfacial mixing, vacancies, and amorphization. To further investigate this, cross-sectional TEM of the specific site was performed and is presented next.

Cross-Sectional TEM

By examining the atomic structure of these samples, we can better understand the resulting PL data. The TEM sample was prepared by FIB lift out. A coating of platinum to protect the surface features mitigated damage caused by the FIB. During final sample thinning, lower beam powers were used to introduce as little ion damage. The final sample was thinned to about 50 nm but was not quite thin enough for electron transparency. Nevertheless, we could see that the sample had several defects present. Figure 5.6 shows many features as marked: a stacking fault starts at the interface and extends through the superlattice above it, small lines on both sides of the interface indicate another type of defect propagating from the FIB irradiation, and there is a dislocation loop on the right side. The stacking fault is 54° to the (001) surface, corresponding to the (111) plane. Stacking faults have been seen previously with ion irradiation.[25]

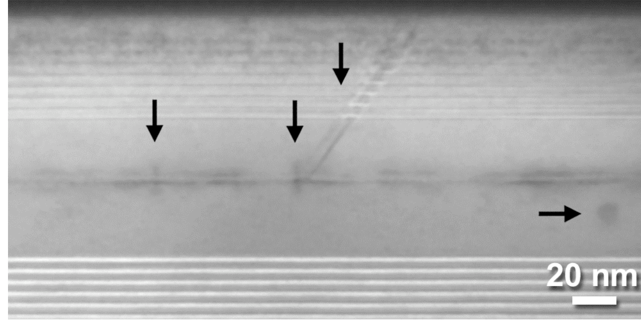

Figure 5.6: Bright field TEM image (2-beam 002 type) of a cross section of the FIB-irradiated PL sample with defects at the interface, a stacking fault, and a dislocation loop marked.

At a different beam condition, another type of defect is shown in Figure 5.7. These spherical defects resemble coffee beans. There is a diffraction contrast from the stress field near a dislocation dipole. These dislocation loops have been commonly seen with quantum dots[31, 36] and many types of ion irradiation in different material systems[18, 22-26]. The dislocation loops are visible 10-20 nm below the interface, which are validated by SRIM calculations. The penetration depth of ions at the 30 kV is 18 ± 10 nm and vacancies extend 30 nm into GaAs.[37] The ion beam causes voids to form these dislocation loops because of the additional strain from the vacancies.

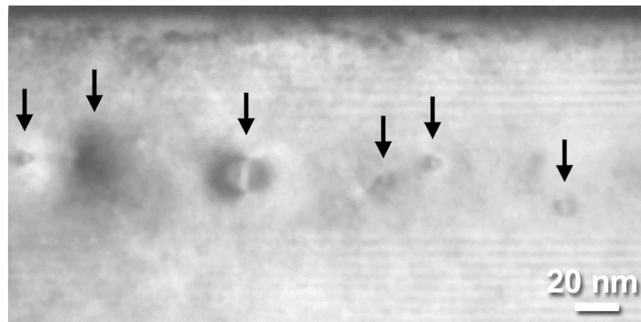

Figure 5.7: Bright field TEM image (2-beam 220 type) of a cross section of the FIB-irradiated PL sample with dislocation dipoles at the interface and below the interface.

There is one more feature that was visible in the TEM and is shown in Figure 5.8. Triangles are seen at the interface and just below the interface. These are a paired set of crystallographic defects that are likely stacking faults. The triangle is 54° to the (001) surface, just like the stacking fault and corresponds to the (111) plane. This triangle defect has been seen in GaAs before and is associated with a defect that causes a pyramidal disruption in the lattice structure.[28-30]

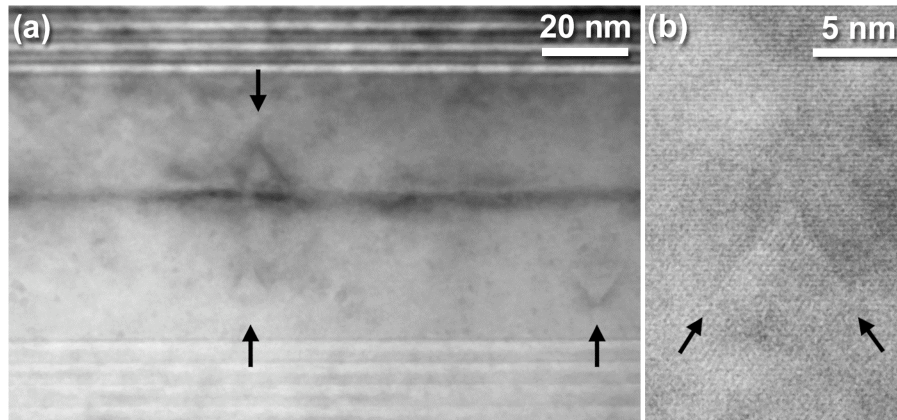

Figure 5.8: Bright field TEM image (2-beam 002 type) of a cross section of the FIB-irradiated PL sample. The images show (a) triangle-shaped defects at the interface or below it and (b) higher resolution image of the defect below the interface. These are most likely stacking faults.

Conclusions

The TEM images presented show many forms of dislocations acting as charge traps to hinder any PL emission. Normal photon radiation is suppressed by disruptions within the lattice. We have shown evidence of this with spatial maps of PL spectra. InAs quantum dot peaks at the edge of the sample were reduced at FIB areas. Future cross-sectional TEM investigations would include examining an ion dose at a single spot to better understand the hole formation, the way they fill, and the defects from the ions.

Annealing at high temperatures could reduce structural defects to obtain stronger PL emission.[33, 38] While this would help with defects, it could also erode the patterns. Minimal annealing time and temperature would have to be achieved to optimize the point at which the PL is active from lowered number of ion defects.

References

[1] Chow W W and Koch S W. *Semiconductor-Laser Fundamentals*. Berlin: Springer; 1999

[2] Vurgaftman I, Meyer J R and Ram-Mohan L R. 2001 *J Appl Phys* **89** 5815-5875

[3] Chu L, Arzberger M, Bohm G and Abstreiter G. 1999 *J Appl Phys* **85** 2355-2362

[4] Henini M, Sanguinetti S, Brusaferri L, Grilli E, Guzzi M, Upward M D, Moriarty P and Beton P H. 1997 *Microelectr J* **28** 933-938

[5] Heitz R, Ramachandran T R, Kalburge A, Xie Q, Mukhametzhanov I, Chen P and Madhukar A. 1997 *Phys Rev Lett* **78** 4071-4074

[6] Tarasov G G, Mazur Y I, Zhuchenko Z Y, Maassdorf A, Nickel D, Tomm J W, Kissel H, Walther C and Masselink W T. 2000 *J Appl Phys* **88** 7162-7170

[7] Schuh D, Bauer J, Uccelli E, Schulz R, Kress A, Hofbauer F, Finley J J and Abstreiter G. 2005 *Physica E* **26** 72-76

[8] Liu H Y, Hopkinson M, Harrison C N, Steer M J, Frith R, Sellers I R, Mowbray D J and Skolnick M S. 2003 *J Appl Phys* **93** 2931-2936

[9] Liu G T, Stintz A, Li H, Malloy K J and Lester L F. 1999 *Electron Lett* **35** 1163-1165

[10] Solomon G S, Trezza J A, Marshall A F and Harris J S, Jr. 1996 *Phys Rev Lett* **76** 952-955

[11] Ishikawa T, Kohmoto S, Nishikawa S, Nishimura T and Asakawa K. 2000 *J Vac Sci Technol B* **18** 2635-2639

[12] Yokota H, Tsunashima K, Iizuka K and Okamoto H. 2008 *J Vac Sci Technol B* **26** 1097-1099

[13] Cheng C C, Meneou K and Cheng K Y. 2009 *Appl Phys Lett* **95** ARTN 173108

[14] Song H Z, Usuki T, Hirose S, Takemoto K, Nakata Y, Yokoyama N and Sakuma Y. 2005 *Appl Phys Lett* **86** ARTN 113118

[15] Meneou K, Cheng K Y, Zhang Z H, Tsai C L, Xu C F and Hsieh K C. 2005 *Appl Phys Lett* **86** ARTN 153114

[16] Atkinson P, Kiravittaya S, Benyoucef M, Rastelli A and Schmidt O G. 2008 *Appl Phys Lett* **93** ARTN 101908

[17] Schneider C, Strauss M, Sunner T, Huggenberger A, Wiener D, Reitzenstein S, Kamp M, Hofling S and Forchel A. 2008 *Appl Phys Lett* **92** ARTN 183101

[18] Barabash R, Ice G, Kroger R, Lohmeyer H, Sebald K, Gutowski J, Bottcher T, Hommel D, Liu W and Chung J S. 2007 *Mater Res Soc Symp P* **1020** 21-27

[19] Bellini E, Taurino A, Catalano M, Lomascolo M, Passaseo A and Vasanelli L. 2009 *Nanotech* **20** ARTN 255306

[20] Mehta M, Reuter D, Melnikov A, Wieck A D and Remhof A. 2007 *Appl Phys Lett* **91** 123108

[21] Myers D R. 1991 *Opt Quant Electron* **23** S985-S994

[22] Pearton S J, Poate J M, Sette F, Gibson J M, Jacobson D C and Williams J S. 1987 *Nucl Instrum Meth B* **19-2** 369-380

[23] Chen S, Lee S T, Braunstein G and Tan T Y. 1989 *Appl Phys Lett* **55** 1194-1196

[24] Millunchick J M, Hultman L and Barnett S A. 1995 *J Vac Sci Technol A* **13** 1155-1159

[25] Myers D R, Dawson L R, Biefeld R M, Arnold G W, Hills C R and Doyle B L. 1988 *Superlattice Microst* **4** 585-589

[26] Ralston J, Wicks G W, Eastman L F, De Cooman B C and Carter C B. 1986 *J Appl Phys* **59** 120-123

[27] Chu C H, Hsieh Y F, Harriott L R and Wade H H. 1991 *J Vac Sci Technol B* **9** 3451-3455

[28] Kakibayashi H, Nagata F, Katayama Y and Shiraki Y. 1984 *Jpn J Appl Phys 2* **23** L846-L848

[29] Tanimura J, Wada O, Endoh Y, Imaizumi M and Ogama T. 1996 *Mater Res Soc Symp P* **399** 485-490

[30] Yen M Y, Madhukar A, Lewis B F, Fernandez R, Eng L and Grunthaner F J. 1986 *Surf Sci* **174** 606-614

[31] Sanchez A M, Beanland R, Hasbullah N F, Hopkinson M and David J P R. 2009 *J Appl Phys* **106** ARTN 024502

[32] Hasbullah N F, Ng J S, Liu H Y, Hopkinson M, David J P R, Badcock T J and Mowbray D J. 2009 *IEEE J Quantum Elect* **45** 79-85

[33] Gierak J, Bourhis E, Jede R, Bruchhaus L, Beaumont B and Gibart P. 2004 *Microelectron Eng* **73-74** 610-614

[34] Mckay H, Rudzinski P, Dehne A and Millunchick J M. 2007 *Nanotech* **18** 455303

[35] Xie Z G and Solomon G S. 2005 *Appl Phys Lett* **87** ARTN 093106

[36] Gutierrez M, Hopkinson M, Liu H Y, Ng J S, Herrera M, Gonzalez D, Garcia R and Beanland R. 2005 *Physica E* **26** 245-251

[37] Zeigler J F, Biersack J and Littmark U. *The Stopping and Ranges of Ions in Matter*. New York: Pergamon; 1985

[38] Taylor C, Marega E, Stach E A, Salamo G, Hussey L, Munoz M and Malshe A. 2008 *Nanotech* **19** ARTN 015301

CHAPTER 6 – Conclusions

Discussion of Work

In this work, assembly in III-V semiconductors has been investigated in different forms. We have examined the morphologies of two systems: mesas in 2 ML GaAs films on $In_{0.53}Ga_{0.47}As$/InP and quantum dots of <2 ML InAs films on GaAs.

In the first material system we show appreciable morphological changes with varying growth parameters. We calculated mesa width changes with temperature. At high growth temperatures, intermixing reduced the strain of the film, as confirmed by X-ray COBRA results. Comparison of the film undulations to the ATG instability shows that the reduction of strain at high temperatures contradicts the decrease in mesa length. At higher temperatures the mesa width decreased as a result of surface energy decreasing, likely caused by desorption of adatoms. We also quantified the roughness in these films by calculating the step edge density from STM images. Significant surface roughening was caused by very low As overpressure. The V:III growth ratio was shown to be an irrelevant growth metric at low As rates. We used a mathematical model of Ga adatom density to correlate the step edge density with the growth variables.

Desorption of *ex situ* FIB-patterned samples proved challenging. To obtain a surface smooth enough for directed quantum dot nucleation required careful calibration of Ga-assisted desorption. Our attention focused on *in vacuo* FIB patterning.

With the InAs on GaAs system, we were able to direct the assembly of quantum dots on FIB-patterned GaAs surfaces. By changing FIB irradiation dose and periodicity along with growth parameters, we were able to obtain single or multiple dots. We looked at elastic KMC simulations to look at the nucleation mechanisms and pair that with our experimental results. This appeared to have good correlation, but the simulations did not allow for enough intermixing and for the hole shape to change. Line profiles showed an enlarged hole diameter after InAs deposition. Characterization of the quantum dots was challenging because of the large range of sizes.

After creating the FIB-patterned quantum dots, PL structures were grown and measured. The InAs peak emission was spatially mapped and was quenched from ion irradiation. TEM images confirmed the presence of defects to decrease PL emission. Stacking faults and dislocation loops were found along the irradiated area. These defects are commonly found in ion irradiated samples. High temperature annealing before InAs deposition could reduce these defects and produce InAs active peaks, but at the expense of delocalizing the InAs quantum dots as shown by Mehta et al.[1]

Future Experiments

The purpose of this work was to manipulate growth parameters and starting surfaces to reliably obtain specific surface features for assembly. In the case of GaAs on $In_{0.53}Ga_{0.47}As/InP$, the terraces could be well characterized by certain growth conditions.

The lattice-matched InGaAs/InP system poses an interesting scenario where equal amounts of strain can be applied both in compression and tension. Future studies could explore the effects of growth parameters on thin films of AlAs, InAs or GaSb on $In_{0.53}Ga_{0.47}As$/InP. Figure 6.1 shows the different STM images associated with various 2 ML films on $In_{0.53}Ga_{0.47}As$/InP. The amount of strain is the same in each case as shown from the difference in lattice parameters in Table 1.1, but the morphologies are very different. The chemical characteristics and bonding energies create vastly different morphologies.

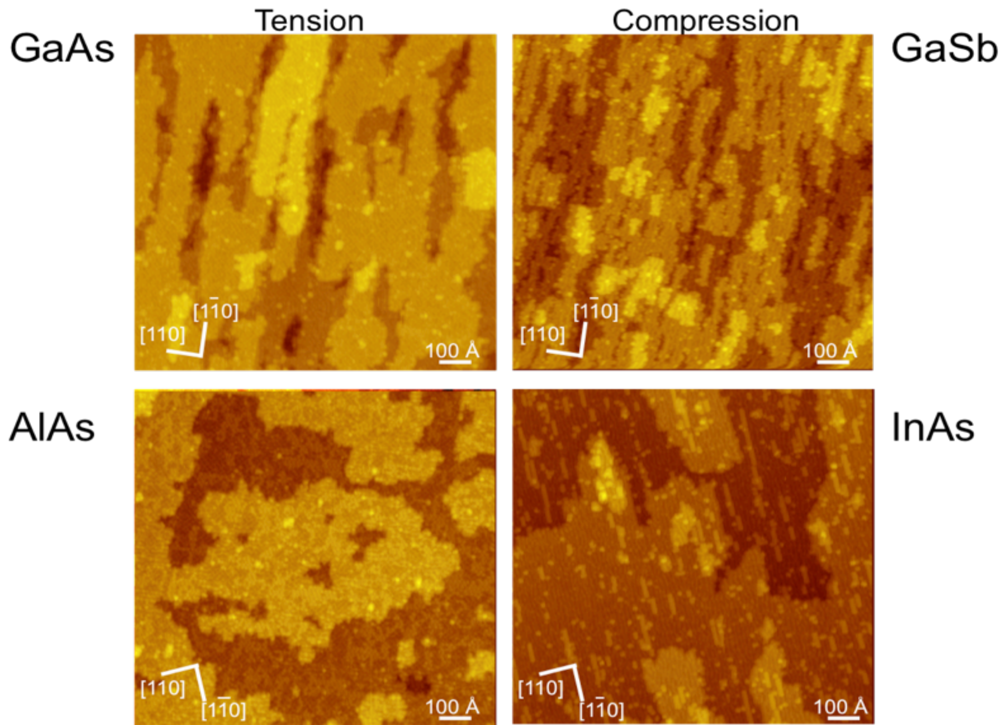

Figure 6.1: STM images of 2 ML on $In_{0.53}Ga_{0.47}As$ / InP(001).

InAs would be fairly straightforward because In is already present within the buffer layer, but the system will now be in compression. The GaSb system should have close results to the GaAs system because it has similar mesa-trench features. The

introduction of Sb may be challenging because it is a quaternary system. Similarly, AlAs may be a very complex structure with the addition of a new element, Al.

In patterning surfaces for quantum dot growth, fine-tuning of growth parameters and patterns to make quantum dots must occur before uniformly sized dots can be achieved.

For patterning of surfaces, if ex situ FIB is available, then we must first calibrate the growth system more systematically to ensure the best starting surface after oxide desorption. H-assisted desorption would be easier to deal with as it was seen to less adversely affect the starting geometry than Ga-assisted desorption.[2] If this could be added to the MBE chamber, that would be a great investment for pursuit of *ex situ* patterning.

Any FIB patterning, inside or outside the chamber, will require an extensive look at annealing to mitigate ion damage. More cross-sectional TEM images will have to be acquired to investigate the defects in the crystal. If the sample shows sign of improved structure, then more micro PL spectra need to be taken. It would be ideal to combine the strengths of the Ku and Sih setups and use the more powerful 532 nm $Nd:YVO_4$ laser in conjunction with the fast steering mirror for spatial mapping. This would allow for more comprehensive studies of the quantum dots as a function of excitation power.

Further, extending the STM to image FIB irradiated areas and see if there are any changes in reconstruction that could be induced from low ion doses should yield interesting results. This is a challenging experiment because it is difficult to image with the STM when the maximum image size is about 200 nm. We would need to develop a method to ensure the STM tip was able to focus on the FIB irradiated region.

The work laid out here shows the potential for controlling films parameters to produce better and more efficient III-V semiconductor devices and also leads to many intriguing paths for future experiments. The short-term focus of these experiments should be defect attenuation via annealing.

References

[1] Mehta M, Reuter D, Melnikov A, Wieck A D and Remhof A. 2007 *Appl Phys Lett* **91** 123108

[2] Atkinson P and Schmidt O G. 2009 *J Cryst Growth* **311** 1815-1818